Modeling of Solidification of Metal-Matrix Particulate Composites with Convection

R.J. FELLER and C. BECKERMANN

A multiphase model for the alloy solidification of metal-matrix particulate composites with convection is developed. Macroscopic transport equations are written for each phase, with unknown parameters modeled through supplementary relations pertinent to the solidification of a binary alloy matrix containing a stationary solid phase and generally nonstationary spherical particles. The model is applied to various one- and two-dimensional systems containing an Al-7 wt pct Si/SiC composite. One-dimensional sedimentation results in nonclustering and clustering particle systems show good agreement with experiments. One-dimensional composite solidification results illustrate the effect of particle clustering and cooling direction on the final macroscopic particle distribution. Two-dimensional results in various unreinforced and reinforced systems illustrate macroscopic particle segregation and its effect on buoyancy-driven melt convection and species macrosegregation. Results indicate a nearly uniform particle distribution for relatively small particles due to negligible particle settling prior to entrapment. For relatively large particles, significant particle settling prior to entrapment results in large denuded and packed zones in the casting. Fluid flow and macrosegregation during solidification are substantially reduced in the presence of particles, due to the relatively large interfacial drag exerted on the liquid by the stationary mush and particle phases.

I. INTRODUCTION

METAL-MATRIX particulate composites (MMPCs) are an important class of materials that exhibit the desirable properties of composites such as low density, damping properties, increased fatigue resistance, and high specific strength, but also are among the least expensive composites to produce *via* molten metal routes.[1,2] General reviews on MMPC solidification can be found in a number of publications.[3,4,5] The macroscopic (*i.e.*, system scale) redistribution of particles during solidification of MMPCs is an important factor influencing final cast properties,[3,6,7] although properties are also affected by the particles' influence on such phenomena as heat transfer, melt convection, species macrosegregation, and microstructure formation. Control of the above phenomena during casting enables the elimination of defects as well as the design of novel materials with spatially varying properties in response to performance requirements. The present study is aimed at modeling the macroscopic particle redistribution and multiphase transport phenomena during solidification of MMPCs.

The casting of MMPCs *via* dispersion processing[8] involves the addition of a reinforcing particle phase (*e.g.*, SiC or graphite particles) to a liquid metal matrix (typically Al alloys) that is subsequently solidified. A wealth of complex physical phenomena may occur in this process, including particle incorporation into the liquid melt, chemical reactions, fluid motion induced by the buoyant motion of the particles, clustering, thermosolutal convection, and multicomponent solidification with and without the presence of particles. The reinforcing phase in MMPC melts is generally mobile, and may be segregated to different regions of the casting due to settling/flotation as well as due to interactions with the advancing semisolid region (*i.e.*, *mushy zone*). Han and Hunt[9,10] found that for a sufficiently small spacing between the primary solid dendrites of the mush, the flow conditions may be such that the particles are prevented from passing through the interface between the fully liquid and mushy regions (*i.e.*, the macroscopic growth front) and instead flow along this ''rough'' interface. On the other hand, for a relatively ''open'' columnar or an equiaxed dendritic mush morphology (the latter being most common in Al alloys), the particles are not rejected by the front and can penetrate into the mushy zone. Once inside the mush, *macroscopic* particle motion is largely prevented by the presence of the microscopically complex solid/liquid interfaces (*i.e.*, dendrites) which entrap the particles. Any particle pushing (review provided by Asthana and Tewari[11]) by the microscopic interfaces in the mush does generally not result in macroscopic particle motion, since the interfaces are converging upon one another. Such pushing will only cause the particles to be ultimately segregated to the grain boundaries, which is a commonly observed phenomenon.

Macroscopic particle segregation during dispersion processing of MMPCs has received limited research attention in the past, in which work has generally focused on particle segregation occurring with and without solidification. Pure particle sedimentation (*i.e.*, without solidification) has been studied extensively in aqueous systems,[12,13] but only a few researchers have addressed this problem in liquid metals. The extent of the denuded zone during isothermal holding of MMPCs has been examined in studies by Rohatgi *et al.*,[14,15] in which Al-Si-based A356 melts containing 14-μm SiC particles were isothermally held and then quenched to determine the extent of the zone. It was observed that

R.J. FELLER, formerly Graduate Research Assistant, Department of Mechanical Engineering, The University of Iowa, is Senior Research Engineer, Caterpillar, Inc., Peoria, IL 61656. C. BECKERMANN, Professor, is with the Department of Mechanical Engineering, The University of Iowa, Iowa City, IA 52242.

Manuscript submitted July 8, 1996.

particle packing occurred at particle concentrations of ~0.25, which is well below that of a close packing of spheres (~0.5). This same phenomenon was observed by Setargew *et al.*,[16] who attributed the rapid observed sedimentation rates to particle clustering, but did not indicate what mechanism was causing such a low packing fraction. Settling experiments in A356/SiC systems were also conducted by Lloyd and Chamberlain,[17] but system dimensions were not given and it was not possible to calculate the final packing fraction. Irons *et al.*[18] studied sedimentation of SiC particles in Al-Si melts using a novel resistance probe to measure the *in situ* volume fraction of particles during sedimentation, and further developed a two-phase model to predict the movement of the settling interfaces. The packing fraction was seen to correspond to that of a close packing of spheres with no apparent clustering, which can be attributed to the relatively large particles (90 μm) used in their work. Particle clustering of SiC particles in A356 melts was studied by Irons and Owusu–Boahen[19] using this same resistance probe. Based on the clustering model of Fouda and Capes,[20] Irons and Owusu–Boahen determined that 14-μm particles formed clusters of ~38-μm diameter with a particle fraction of ~0.42 within the cluster, although these numbers were found to be dependent upon the amount of stirring prior to sedimentation. The clusters were found to pack at a volume fraction equal to that of a random close-packed collection of equivalently sized spheres (~0.6). Since the clusters had an internal particle fraction of ~0.42, the actual particle packing fraction (~0.25 = 0.6 × 0.42) corresponded to that found earlier by Rohatgi *et al.* and Setargew *et al.* Han and Hunt[9,10] have investigated particle rejection as a result of fluid flow in the absence of solidification. Through experimentation, it was proposed that critical geometrical and velocity ratios exist such that particles would be rejected by a rough interface.

Macroscopic particle segregation with solidification has been studied both experimentally and theoretically, the latter of which generally involves the incorporation of microscopic particle pushing/engulfment transition models[11] into solidification simulation codes. Sasikumar and Pai[21] developed a simple computer model that compared predetermined local solidification times to particle motion, based on Stokes terminal particle velocity, to determine macroscopic particle segregation in a casting. A considerably more advanced approach was undertaken by Sasikumar and Kumar,[22] in which macroscopic particle segregation in a pure-substance matrix was further modeled through the inclusion of pushing/engulfment transitions based on an extension of a critical velocity expression developed by the same researchers.[23] The front velocity calculated from a heat-conduction model was compared to this critical velocity expression to determine whether pushing or engulfment of the particles by the planar interface occurred. Stefanescu *et al.* also examined macroscopic particle segregation through computer modeling,[24,25] in which critical velocity expressions developed by this group[26,27] were compared to predetermined interface velocities to predict pushing/engulfment transitions in pure-substance matrices containing macroscopically planar interfaces and otherwise stationary particles. Stefanescu *et al.*[26,28] also carried out several experiments to provide comparison data for the theoretical model. Experiments were generally conducted in Bridgman-type furnaces, in which Al composites containing SiC and graphite particles were directionally solidified with various furnace translation rates and temperature gradients. For composites in which the solidification direction was parallel to the gravity vector, denuded and packed zones were generally observed near the extremities of the samples, which was attributed to sedimentation/flotation prior to solidification. Particle entrapment was generally observed for the case where the gravity vector was antiparallel to the solidification direction, although in certain cases, a banded structure consisting of alternating regions of high and low particle fractions was observed. This phenomenon occurred at relatively low particle fractions and front velocities, and was attributed to periodic accumulation and entrapment of particles as the particle fraction in front of the interface increased. In other experiments utilizing an Al-Cu/SiC system for which the gravity vector was antiparallel to the solidification direction,[29] the relatively dense particles were found to accumulate in the upper region of the casting, which was attributed to particle floatation caused by gas absorption around the particles during mixing. Lloyd[30] observed a region devoid of particles near the chill during solidification of A356/SiC bottom-cooled systems, and attributed this phenomenon to pushing by an essentially planar interface in this region which could physically push the particles. Similar phenomena were observed by Rohatgi *et al.* in solidification experiments utilizing A357/SiC[31,32] and A356/SiC[33] systems cooled from below, although particles were macroscopically pushed for nearly the entire length of the casting in the former case, but only very near the chill in the latter. Rohatgi *et al.* also developed a one-dimensional heat-transfer model to investigate the effect of stationary particles on temperature profiles and interface velocities in a pure-substance matrix.[34] Particle settling concurrent with alloy solidification has very recently been modeled by Hanumanth and Irons,[35] who compared results of a one-dimensional enthalpy model to experiments in A356/SiC systems. In their model, particle settling and mushy zone evolution were accounted for using the Richardson–Zaki hindered settling correlation and Scheil equation, respectively. It was proposed that the SiC particle thermal conductivity should be on the order of the single crystal value for accurate representation of cooling rates and particle settling, although very little settling was found to occur for the prescribed cooling rates.

In an effort to incorporate in a model fundamental information regarding the interactions between phases in a system, a number of researchers in the area of multiphase flows have employed the so-called continuum approach, where each phase in the system is described as a continuum, occupying the same region in space.[13,36] In this approach, macroscopic conservation equations are written for each phase, with interfacial terms modeled based on the system under study. This approach has been applied to the modeling of fluid-particulate systems[18,37–41] as well as solidification of unreinforced multicomponent mixtures (referenced by Beckermann and Wang[42]). The incorporation of liquid-particulate flow and alloy (*i.e.*, dendritic) solidification into a single, comprehensive model has not been done in the past, and this is the purpose of the current study.

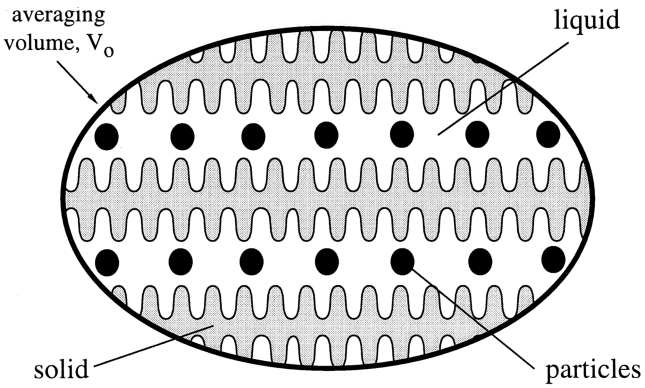

Fig. 1—A typical averaging volume containing liquid, solid, and particles.

The objectives of this work are to develop a model to predict the multiphase transport occurring during alloy solidification of MMPCs and to illustrate the ability of the model to predict macroscopic particle segregation during solidification of various MMPC systems. It is assumed that particles are always entrapped by an advancing mush, limiting the model to an equiaxed or relatively open columnar dendritic microstructure. Although the primary focus of this work is the investigation of macroscopic particle transport, the effect of particle transport on other variables (*e.g.*, fluid flow, macrosegregation, and temperature) is also investigated. In Section II, the model equations are developed with main assumptions outlined. This is followed by a brief description of the numerical solution procedure. Results are then presented for one-dimensional sedimentation and solidification as well as for two-dimensional solidification in various Al-7 wt pct Si/SiC systems.

II. MODEL DESCRIPTION

The general multiphase macroscopic mass, momentum, energy, and species conservation equations, and associated interfacial balances, can be found in a number of publications[43,44] and are not repeated here. Such volume-averaged equations are obtained by averaging the corresponding microscopic (*i.e.*, exact) equations for each phase over an averaging volume, V_0, that is small compared to the system but large compared to the interfacial structures it contains. In the present context, a ''phase'' refers to a distinct component in the system such as the liquid, solid, and particle phases shown in the typical averaging volume of Figure 1. The details of the averaging process, including the exact expressions for the interfacial transfers (written in terms of integrals over the interfacial areas) and macroscopic fluxes, can be found in the original references.

The governing equations for the solidification of MMPCs are obtained by applying the volume-averaged macroscopic conservation equations to a specific system and modeling the unknown parameters through development of supplementary relations. The final equations are shown in Table I. In all equations, ε_k and Ψ_k represent the volume fraction and intrinsic volume average of a quantity Ψ of phase k, respectively, while $\overline{\Psi}_{kj}$ indicates an average of a quantity Ψ of phase k over the k/j interfacial area in the averaging volume. All other symbols are defined in the Nomenclature. The main assumptions employed are as follows (others can be found in earlier articles[43,44]).

(1) The phases contained in the system are liquid, solid, and particle (*i.e.*, porosity is neglected). It then follows that

$$\varepsilon_l + \varepsilon_s + \varepsilon_p = 1 \qquad [1]$$

Note that the equations in Table I contain an additional phase, namely the bulk solid phase, which is a combined solid and particle phase as described in Section III.

(2) The solid (but not the particle) phase is rigid and stationary (*i.e.*, $\mathbf{v}_s = 0$). As a result, the model is limited to the solidification of a columnar microstructure that is attached to the wall, but it also applies to an equiaxed microstructure in which the solid phase can be assumed to be stationary.

(3) The particles are rigid and spherical, do not change phase, are of constant composition, and do not react with the matrix (*i.e.*, the particles are inert). Further, the particles are assumed to be uniformly distributed in an initially quiescent melt prior to solidification (*i.e.*, residual velocities left over from filling are not considered). Particle incorporation into the liquid melt is not considered in this work.

(4) Particles are immediately entrapped locally at the onset of local solidification (*i.e.*, no particle rejection occurs at the mush/liquid interface).

(5) Local thermal equilibrium exists, which is justified by the typically large Lewis number of metal alloys and the relatively small particles used in MMPCs.

(6) The liquid within an averaging volume is solutally well mixed, *i.e.*,

$$C_l = \overline{C}_{ls} \qquad [2]$$

Further, finite-rate macroscopic liquid species diffusion is included, while microscopic solid species diffusion (*i.e.*, $\tilde{D}_{sl}$) is modeled by assuming a one-dimensional platelike model of the solid dendrite and assuming a parabolic concentration distribution in the solid.[45]

(7) Thermodynamic equilibrium exists at the solid/liquid interface so that temperature and concentration may be related through an equilibrium phase diagram.

(8) All macroscopic transport properties (*e.g.*, thermal conductivities and solutal diffusivities) are taken as their microscopic counterparts, with the exception of the macroscopic viscosities (refer to Section II–B).

(9) Secondary and primary arm spacing expressions (*i.e.*, λ_2 and λ_1) for unreinforced Al-Si alloys[33,46] are assumed to apply to all reinforced matrices in this study.

(10) Gravity is the only external force acting on the system.

(11) All thermophysical properties are assumed to be constant except for the liquid density in the liquid buoyancy term, where it is allowed to vary with temperature and concentration (to account for thermosolutal convection). Contraction-driven flow is neglected.

Relations are presented in the following sections for the unknown parameters in Table I, including relations for the dissipative interfacial stresses, the macroscopic viscosities, and particle clustering. A summary is given in Table II.

A. *Dissipative Interfacial Stresses*

The dissipative interfacial stresses (*i.e.*, interfacial drag) in the momentum equations account for the interfacial mo-

Table I. Summary of the Macroscopic Conservation Equations

Mass conservation

Liquid
$$\frac{\partial}{\partial t}(\varepsilon_l \rho_l) + \nabla \cdot (\varepsilon_l \rho_l \mathbf{v}_l) = -\frac{\partial}{\partial t}(\varepsilon_s \rho_s)$$

Bulk solid
$$\frac{\partial}{\partial t}(\varepsilon_b \rho_b) + \nabla \cdot (\varepsilon_b \rho_b \mathbf{v}_b) = \frac{\partial}{\partial t}(\varepsilon_s \rho_s)$$

Momentum conservation

Liquid
$$\varepsilon_l \rho_l \frac{\partial \mathbf{v}_l}{\partial t} + \varepsilon_l \rho_l \mathbf{v}_l \cdot \nabla \mathbf{v}_l = -\varepsilon_l \nabla P - \varepsilon_l \rho_l^{\text{ref}} [\beta_T (T - T^{\text{ref}}) + \beta_C (C_l - C_l^{\text{ref}})] \mathbf{g} + \mathbf{v}_l \frac{\partial}{\partial t}(\varepsilon_s \rho_s) + \nabla \cdot \{\varepsilon_l \mu_l [\nabla \mathbf{v}_l + (\nabla \mathbf{v}_l)^t]\} + \nabla \cdot \left\{ \mu_l \left[\left(\mathbf{v}_l - \frac{\varepsilon_b \rho_b}{\varepsilon_p \rho_p} \mathbf{v}_b \right) \nabla \varepsilon_l + \nabla \varepsilon_l \left(\mathbf{v}_l - \frac{\varepsilon_b \rho_b}{\varepsilon_p \rho_p} \mathbf{v}_b \right) \right] \right\} - \beta_{ls} \mathbf{v}_l + \beta_{lp} \left(\frac{\varepsilon_b \rho_b}{\varepsilon_p \rho_p} \mathbf{v}_b - \mathbf{v}_l \right)$$

Bulk solid
$$\varepsilon_b \rho_b \frac{\partial \mathbf{v}_b}{\partial t} + \varepsilon_b \rho_b \mathbf{v}_b \cdot \nabla \mathbf{v}_b = -\varepsilon_b \nabla P + \varepsilon_s \nabla P + \varepsilon_b (\rho_b - \rho_l^{\text{ref}}) \mathbf{g} - \mathbf{v}_b \frac{\partial}{\partial t}(\varepsilon_s \rho_s) + \nabla \cdot \left\{ \varepsilon_p \mu_p \left[\nabla \left(\frac{\varepsilon_b \rho_b}{\varepsilon_p \rho_p} \mathbf{v}_b \right) \right] + \varepsilon_p \mu_p \left[\nabla \left(\frac{\varepsilon_b \rho_b}{\varepsilon_p \rho_p} \mathbf{v}_b \right) \right]^t \right\} - \nabla \cdot \left[\frac{\varepsilon_s \rho_s}{\varepsilon_p \rho_p} \varepsilon_b \rho_b \mathbf{v}_b \mathbf{v}_b \right] - \beta_{ps} \frac{\varepsilon_b \rho_b}{\varepsilon_p \rho_p} \mathbf{v}_b + \beta_{lp} \left(\mathbf{v}_l - \frac{\varepsilon_b \rho_b}{\varepsilon_p \rho_p} \mathbf{v}_b \right)$$

Mixture energy conservation
$$[\varepsilon_l \rho_l c_l + \varepsilon_s \rho_s c_s + \varepsilon_p \rho_p c_p] \frac{\partial T}{\partial t} + [\varepsilon_l \rho_l c_l \mathbf{v}_l + \varepsilon_b \rho_b c_p \mathbf{v}_b] \cdot \nabla T = \nabla \cdot [(\varepsilon_l k_l + \varepsilon_s k_s + \varepsilon_p k_p) \nabla T] + [(c_s - c_l)(T_M - T) + \Delta h_M] \frac{\partial}{\partial t}(\varepsilon_s \rho_s)$$

Liquid and solid species conservation

Liquid
$$\varepsilon_l \rho_l \frac{\partial C_l}{\partial t} + \varepsilon_l \rho_l \mathbf{v}_l \cdot \nabla C_l = \nabla \cdot (\varepsilon_l \rho_l D_l \nabla C_l) + (C_l - C_s) \frac{\partial}{\partial t}(\varepsilon_s \rho_s) - \varepsilon_s \rho_s \frac{\partial C_s}{\partial t}$$

Solid
$$\varepsilon_s \rho_s \frac{\partial C_s}{\partial t} = (\overline{C}_{sl} - C_s) \left[\frac{\partial}{\partial t}(\varepsilon_s \rho_s) + \tilde{D}_{sl} \right]$$

mentum exchange between phases k and j due to relative motion between the phases. These terms are modeled as the product of an interfacial momentum exchange coefficient, β_{kj}, and the difference between the average and interfacial velocities of phase k. In the current system, relations are required for β_{lp}, β_{ls}, and β_{ps}. These quantities are modeled in the following equations.

1. *Liquid-particle drag*

The liquid-particle momentum exchange coefficient β_{lp} may be modeled similar to that in Gidaspow,[38] where a liquid-particle drag coefficient, C_D, in addition to a so-called hindered-settling function, $f(\varepsilon_l)$, is introduced into β_{lp} as

$$\beta_{lp} = \frac{3}{4} \frac{\varepsilon_p}{d_p} \frac{\varepsilon_l^2 \rho_l C_D}{f(\varepsilon_l)} |\mathbf{v}_p - \mathbf{v}_l| \quad [3]$$

where C_D is given by Stokes law in the creeping-flow regime (*i.e.*, $\text{Re}_p < 0.1$) as

$$C_D = \frac{24}{\text{Re}_p} \quad [4]$$

and Re_p is the particle Reynolds number given as

$$\text{Re}_p = \frac{\rho_l d_p |\mathbf{v}_p - \mathbf{v}_l|}{\mu_l} \quad [5]$$

The hindered settling function $f(\varepsilon_l)$ takes into account the effect of multiple particles on the relative velocity. The general definition of $f(\varepsilon_l)$ is given as

$$f(\varepsilon_l) = \frac{\varepsilon_l (\mathbf{v}_p - \mathbf{v}_l)}{V_\infty} \quad [6]$$

where V_∞ is the well-known Stokes settling velocity of a single particle, given as

$$V_\infty = \frac{d_p^2 (\rho_l - \rho_p) g}{18 \mu_l} \quad [7]$$

Substituting Eqs. [4] and [5] into Eq. [3] results in

$$\beta_{lp} = \frac{18 \mu_l \varepsilon_l^2 \varepsilon_p}{d_p^2 f(\varepsilon_l)} \quad [8]$$

A number of expressions for the hindered-settling function $f(\varepsilon_l)$ exist in the literature, including the empirical expression given by Richardson and Zaki:[47]

$$f(\varepsilon_l) = \varepsilon_l^{4.65} \quad [9]$$

which is generally valid in the free-particle regime and the free-surface cell model attributed to Happel,[48] which is given as

$$f(\varepsilon_l) = \frac{2 - 3\eta + 3\eta^5 - 2\eta^6}{2 + \frac{4}{3}\eta^5} \qquad \eta = (1 - \varepsilon_l)^{1/3} \quad [10]$$

Other models for $f(\varepsilon_l)$ are summarized in a number of publications.[49,50,51] Dimensionless β_{lp} are plotted in Figure 2 using both the Richardson–Zaki and Happel hindered-settling functions, with the Blake–Kozeny result[52] for a packed bed of spheres included as a reference. It can be

Table II. Summary of the Supplementary Relations

Interfacial momentum exchange

$$\beta_{lp} = \frac{18\mu_l \varepsilon_l^2 \varepsilon_p}{d_p^2 f(\varepsilon_l)} \qquad f(\varepsilon_l) = \frac{2 - 3\eta + 3\eta^5 - 2\eta^6}{2 + \frac{4}{3}\eta^5} \qquad \eta = (1 - \varepsilon_l)^{1/3} \text{ [48]}$$

$$\beta_{ls} = \frac{\mu_l}{K_1 \lambda_1^2} \frac{(1 - \varepsilon_l)\varepsilon_s}{\varepsilon_l} \qquad \beta_{ps} \to \infty \ (\varepsilon_s \text{ and } \varepsilon_p > 0)$$

Interfacial species exchange[45]

$$\tilde{D}_{sl} = \frac{S_{sl}\rho_s D_s}{l_{sl}} \qquad S_{sl} = 2/\lambda_2 \qquad l_{sl} = \frac{\varepsilon_s \lambda_2}{6}$$

Macroscopic particle viscosity

$$\mu_p = \frac{\mu_m - \varepsilon_l \mu_l}{\varepsilon_p} \qquad \mu_m = \mu_l \left[1 - \frac{\varepsilon_p}{\varepsilon_{pm}}\right]^{-2.5\varepsilon_{pm}} \text{ [68]}$$

Interfacial equilibrium relations[44]

$$C_l = (T - T_M)/m_l$$

$$\overline{C}_{sl} = \begin{cases} \kappa C_l & \text{primary solidification} \\ C_E & \text{eutectic reaction} \\ C_s & \text{local remelting} \end{cases}$$

Bulk solid definitions

$$\varepsilon_b = \varepsilon_s + \varepsilon_p$$
$$\varepsilon_b \rho_b = \varepsilon_s \rho_s + \varepsilon_p \rho_p$$
$$\varepsilon_b \rho_b \mathbf{v}_b = \varepsilon_p \rho_p \mathbf{v}_p$$

Cluster definitions

$$\varepsilon_{pi} = \varepsilon_p / \varepsilon_c$$
$$\rho_c = \varepsilon_{pi}\rho_p + (1 - \varepsilon_{pi})\rho_l$$
$$k_c = \varepsilon_{pi} k_p + (1 - \varepsilon_{pi}) k_l$$
$$c_c = \varepsilon_{pi} c_p + (1 - \varepsilon_{pi}) c_l$$

Tangential wall particle velocity[80]

$$\langle \mathbf{v}_p \rangle^p = -\lambda_p \frac{\partial \langle \mathbf{v}_p \rangle^p}{\partial n} \qquad \lambda_p = \frac{d_p}{\varepsilon_p^{1/3}}$$

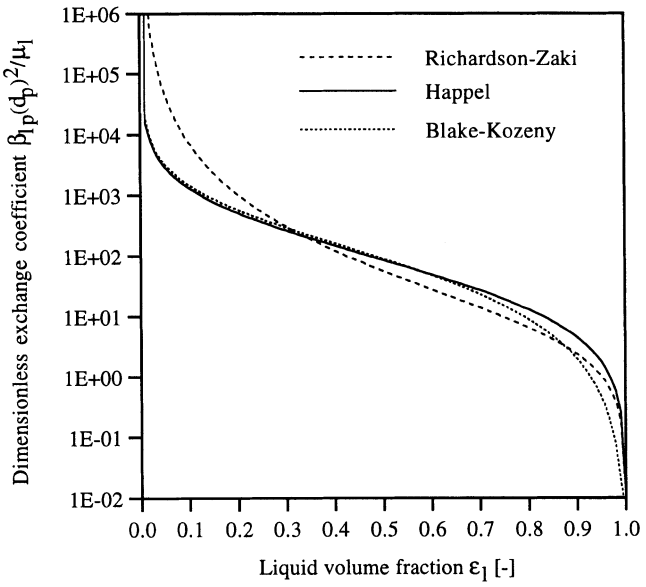

Fig. 2—Dimensionless liquid-particle momentum exchange coefficients using the Richardson-Zaki,[47] Happel,[48] and Blake-Kozeny[52] hindered settling functions.

seen that significant differences exist between the Happel and Richardson–Zaki expressions, but good agreement is found between the Happel and Blake–Kozeny expressions in the Blake–Kozeny range of validity ($\varepsilon_l < 0.5$). The Happel expression also provides a good approximation in the free-particle regime,[53] although it was not expressively derived for this purpose. Hence, the Happel expression is utilized in this study for all liquid fractions.

2. *Liquid-solid drag*

The liquid-solid momentum exchange coefficient β_{ls} is modeled by viewing the stationary mushy zone as a porous medium. Then, a permeability can be introduced in analogy with Darcy's law[54] as

$$\beta_{ls} = \frac{\mu_l \varepsilon_l^2}{K_{ls}} \qquad [11]$$

where K_{ls} [m^2] is the liquid-solid permeability. The term K_{ls} is generally a function of the solidification morphology (*e.g.*, columnar or equiaxed), the volume fractions, and the microstructure. The isotropic Kozeny–Carman model has been used extensively in modeling the permeability in mushy zones (as referenced by Beckermann and Wang[42]), and can be written as

$$K_{ls} = K_0 \frac{\varepsilon_l^3}{\varepsilon_s^2} \qquad [12]$$

where K_0 is a function of the solid microstructure only. Here, K_0 is taken as

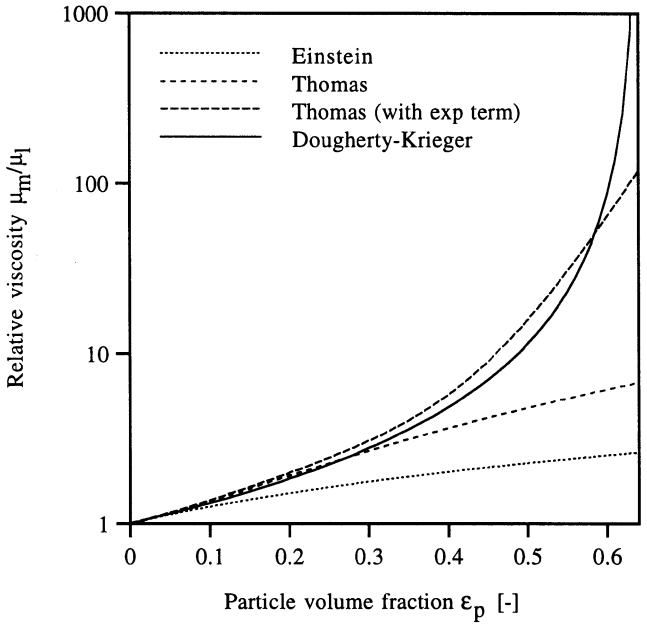

Fig. 3—Relative viscosity of a liquid-particle suspension using the Newtonian mixture viscosity models of Einstein,[65] Thomas,[66] and Dougherty-Krieger.[68]

$$K_0 = K_1 \lambda_1^2 \qquad [13]$$

where $K_1 \approx 6 \times 10^{-4}$ provides a reasonable fit of experimental data[55] in columnar dendritic systems, although the accuracy of the preceding expression is not known.

Upon substitution of Eqs. [12] and [13] into Eq. [11],

$$\beta_{ls} = \frac{\mu_l}{K_1 \lambda_1^2} \frac{\varepsilon_s^2}{\varepsilon_l} \qquad [14]$$

A polydisperse form of Eq. [14] is needed because particles can be present in the mushy zone. This can be accomplished by linearizing β_{ls} with respect to the dispersed-phase volume fraction ε_s, as was done by Shih *et al.*,[56] so that Eq. [14] is modified as

$$\beta_{ls} = \frac{\mu_l}{K_1 \lambda_1^2} \frac{(1 - \varepsilon_l)\varepsilon_s}{\varepsilon_l} \qquad [15]$$

Note that Eq. [8] for the liquid-particle drag is already linear in the particle volume fraction, and can thus be used in the presence of the solid phase. With both Eqs. [8] and [15] linear in the dispersed-phase volume fractions, the total drag force on the liquid is properly calculated as the sum of the drag forces exerted by the particles and the solid.

3. *Particle-solid drag*

The particle-solid momentum exchange coefficient β_{ps} is taken as infinity when solid and particles coexist locally, *i.e.*,

$$\beta_{ps} = \begin{cases} \infty & \varepsilon_s \text{ and } \varepsilon_p > 0 \\ 0 & \varepsilon_s \text{ or } \varepsilon_p = 0 \end{cases} \qquad [16]$$

This approximation implies that $\mathbf{v}_p$ must approach zero, since the particle-solid drag must remain finite, and enables the modeling of immediate particle entrapment within a mush (*i.e.*, assumption (4)). Particle entrapment is, in fact, predicted for all of the current systems based on the approximate model of Han and Hunt,[9,10] because the predicted dendrite arm spacings are large relative to the particle diameters.

B. *Macroscopic Viscosities*

The macroscopic viscosities μ_l and μ_p, appearing in the viscous terms of the momentum equations, represent the rheological behavior of a multiphase system and are necessary parameters in determining the stress on each phase under a given flow situation. The macroscopic solid viscosity μ_s is not required in this work since the solid momentum equation is not considered, due to the assumption of a stationary solid phase. There exists a wide body of literature on the subject of suspension rheology,[57–61] in which the ultimate goal is the determination of the mixture suspension viscosity μ_m. In this work, Newtonian behavior is assumed, for which the suspension viscosity is independent of the shear rate. Non-Newtonian behavior, such as that due to the formation of shear-sensitive particle flocs or interlocking solid dendrites around particles (*e.g.*, during *compocasting*[62,63,64]), is not considered here.

The usual starting point in suspension viscosity is the seminal work of Einstein,[65] who derived the following mixture viscosity for an infinitely dilute suspension of noninteracting spheres in a Newtonian liquid:

$$\mu_m = \mu_l [1 + 2.5 \varepsilon_p] \qquad [17]$$

Einstein's equation is restricted to the particle concentration range in which there is no overlap between the perturbations in the flow field caused by different particles, which is on the order of particle concentrations of 0.01 or less.[66] Many researchers in the MMPC area[27,28,67] have utilized this expression in calculation of a so-called critical velocity, V_{cr}, for particle pushing, in which the viscosity is used to account for the decrease in V_{cr} brought about by an increase in the particle concentration.

Expressions for μ_m that cover a wide range of ε_p are generally empirical, such as that of Thomas,[66]

$$\mu_m = \mu_l [1 + 2.5 \varepsilon_p + 10.05 \varepsilon_p^2 + 0.00273 \exp (16.6 \varepsilon_p)] \qquad [18]$$

as well as semiempirical, such as the Dougherty–Krieger equation,[68]

$$\mu_m = \mu_l \left[1 - \frac{\varepsilon_p}{\varepsilon_{pm}}\right]^{-2.5 \varepsilon_{pm}} \qquad [19]$$

where ε_{pm} is the particle volume fraction at packing. Note that both expressions reduce to Einstein's equation as $\varepsilon_p \to 0$ and include the effect of increasing viscosity for increasing particle concentration. The latter expression, however, explicitly includes the effect of an infinite mixture viscosity at packing (*i.e.*, $\varepsilon_p \to \varepsilon_{pm}$). The Thomas expression, with the exclusion of the exponential term, has also been incorporated into critical velocity expressions by a number of researchers.[24,26,69–71] The previous three models are compared in Figure 3, where the relative mixture viscosity is plotted based on a random packing fraction of $\varepsilon_{pm} = 0.637$. It can be seen that the Thomas and Dougherty–Krieger expressions agree at relatively low particle concentrations, although there is considerable deviation at higher

concentrations. The Dougherty–Krieger relation appears to be the best expression over the entire particle fraction range due to its proper limiting value as packing is reached, and is utilized in the current study.

In a method similar to Wang *et al.*[72] and Ni and Beckermann,[73] the mixture viscosity may be related to the individual phase viscosities, needed in the momentum equations in Table I, by writing μ_m as a phase-average quantity, *i.e.*,

$$\mu_m = \varepsilon_l \mu_l + \varepsilon_p \mu_p \quad [20]$$

This very approximate model is based on the assumptions that the liquid viscosity is equal to its microscopic counterpart and that the relative velocity between the liquid and particles is small. Equation [20] can then be solved for μ_p as

$$\mu_p = \frac{\mu_m - \varepsilon_l \mu_l}{\varepsilon_p} \quad [21]$$

where μ_m is given by the Dougherty–Krieger equation (Eq. [19]).

C. *Particle Clustering Model*

Particle clustering is examined during certain simulations in this work, in which the particle clustering model of Fouda and Capes[20] is utilized. In this model, particles of diameter d_p are assumed to take the form of clusters of diameter $d_c > d_p$ that contain a portion of immobilized liquid that moves with the cluster. The clusters are then viewed as particles with an internal particle fraction, ε_{pi}, given as

$$\varepsilon_{pi} = \frac{\varepsilon_p}{\varepsilon_c} \quad [22]$$

The liquid fraction within the cluster ε_{lc} is calculated by taking the difference between the cluster and particle volume fractions, *i.e.*,

$$\varepsilon_{lc} = (1 - \varepsilon_{pi})\varepsilon_c = \frac{(1 - \varepsilon_{pi})\varepsilon_p}{\varepsilon_{pi}} \quad [23]$$

With this model, the hindered-settling functions as described earlier (within the interfacial drag) can be used to predict the motion of the cluster if the particle quantities are viewed as cluster quantities (as defined in Table II), where an iterative procedure is required to adjust d_c and ε_{pi} to match observed settling rates. Irons and Owusu–Boahen[19] reported values of d_c and ε_{pi} as 38 μm and 0.42, respectively, for clustering of 14-μm SiC particles in an A356 Al-Si alloy, although it was noted that these quantities are dependent upon the amount of stirring prior to solidification. These quantities are assumed to be valid in this work.

III. NUMERICAL IMPLEMENTATION

The numerical implementation procedure is detailed in Feller,[74] and only a brief discussion is given here. The mass- and momentum-conservation equations shown in Table I are written in terms of so-called bulk solid quantities (with a subscript *b*), as defined in Table II. These quantities represent that of a combined solid and particle phase, and are introduced so that the equations may be written in a two-phase (namely, the liquid and bulk solid) framework, as required by available two-phase CFD (computational fluid dynamics) codes. Such a reduction is possible because the solid phase is assumed to be stationary. It is pointed out that the complete set of equations are generally valid regardless of the phases present, since the bulk solid quantities reduce to particle (or solid) quantities in the absence of solid (or particles).

The conservation equations are solved using a fixed-grid, single-domain numerical solution procedure. A fully implicit, control-volume based finite-difference method is utilized to discretize the equations, with the upwind scheme used to evaluate the finite-difference coefficients. The velocity-pressure coupling in the momentum equations is handled using the so-called interphase slip algorithm.[75] The solid volume fraction ε_s is calculated through a coupling of the discretized energy and species equations in the mushy zone, along with phase diagram relations.[76,77] Once the bulk solid and solid quantities are known, the particle quantities may be backed out from the bulk solid definitions given in Table II. At the eutectic point, the energy equation becomes uncoupled from the species equations, and the energy equation alone can be used to calculate ε_s.

Validation of the numerical code implementation was performed through comparison of one- and two-dimensional unreinforced solidification results[74] to those of the binary columnar solidification code (with melt convection and macrosegregation) of Schneider and Beckermann.[77] This code has shown good agreement with existing solutions in the literature. Comparisons of one-dimensional sedimentation results to experiments from the literature are presented in Section IV. Validation of the heat transfer and settling parts of the model for composite solidification can, in principle, be found in Hanumanth and Irons,[35] since the current model essentially reduces to their model for one-dimensional conditions, as discussed subsequently.

Computations for the one-dimensional simulations were performed on grids containing 100 (sedimentation) and 120 (solidification) control volumes in the *y* direction with a single control volume in the *x* direction. Computations for the two-dimensional simulations were performed on a grid that contains 40 control volumes in the *x* direction and 60 control volumes in the *y* direction. Previous experience has shown that such a grid is able to capture all dynamic solidification features at a reasonable computational cost.[78] Time steps of 2.5 and 1 second were utilized for the one-dimensional sedimentation and solidification simulations, respectively, while a time-step of 0.05 seconds was used for the two-dimensional simulations. Calculations were performed on an HP* J200 workstation, in which 1 second of simulation time required approximately 0.4, 25, and 1440 seconds of central processing unit time, respectively, for the preceding three kinds of simulations. Note that the two-dimensional simulation computational times are comparable with those for the unreinforced case obtained by Schneider and Beckermann.[79]

IV. RESULTS AND DISCUSSION

Results are presented for sedimentation and solidification in one- and two-dimensional systems; the physical systems

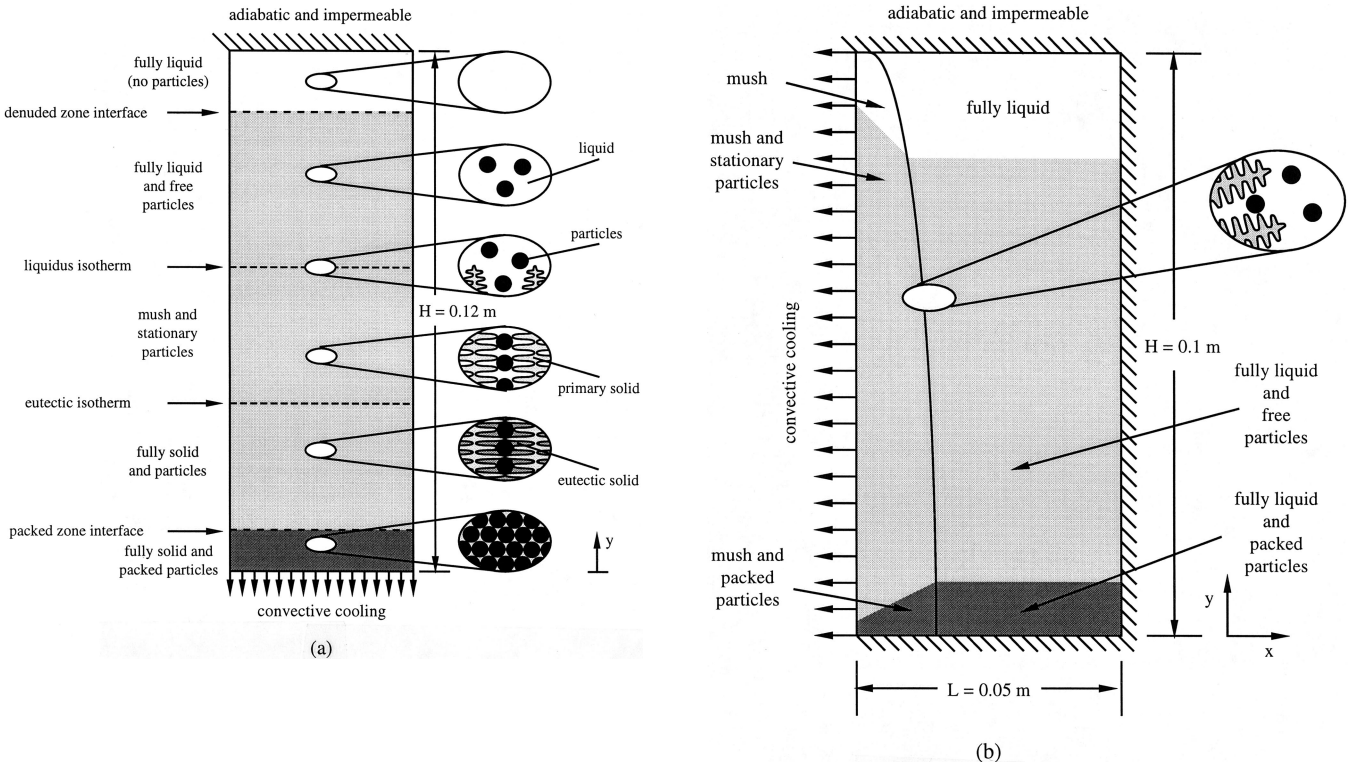

Fig. 4—Schematic illustration of the domain and boundary conditions (shading indicates particle concentration): (*a*) one- and (*b*) two-dimensional systems. The one-dimensional system figure shown is for bottom cooling only.

Table III. Summary of the Simulation Parameters

Simulation	U (W/m²/K)	Cooling	ε_{po} (—)	d_p (μm)	d_c (μm)	ε_{pi} (—)
S1	0	—	0.20	90	90	1
S2	0	—	0.05	14	38	0.42
S3	0	—	0.15	14	38	0.42
C1	500	bottom	0.05	14	38	0.42
C2	500	bottom	0.05	14	14	1
C3	500	top	0.05	14	38	0.42
C4	500	top	0.05	14	14	1
I	250	side	0	—	—	—
II	250	side	0.20	14	14	1
III	250	side	0.20	100	100	1

utilized are illustrated in Figure 4. In all simulations, an initially quiescent binary alloy matrix of uniform temperature T_0 and concentration C_0 contains an initially uniform distribution of monodisperse particles of diameter d_p and volume fraction ε_{po}. A single wall is subjected to convective cooling from a coolant at temperature T_a = 293.2 K and heat transfer coefficient U. The remaining walls are considered adiabatic, with all walls assumed to be impermeable. The velocity boundary conditions are a zero normal component velocity for all phases, a no-slip tangential velocity for the liquid phase, and a partial-slip tangential velocity (Table II) for the particle (*i.e.*, bulk solid) phase. A complete-slip tangential velocity is allowed for both phases in the one-dimensional simulations.

A summary of the parameters used in each simulation is given in Table III, with the thermophysical properties and empirical constants used given in Table IV. Cases S1 to S3 involve one-dimensional sedimentation of nonclustering (*i.e.*, ε_{pi} = 1) and clustering (*i.e.*, ε_{pi} <1) particles of various initial particle concentrations. Sedimentation coupled with solidification is examined in cases C1 to C4, in which one-dimensional systems containing clustering or nonclustering particles are cooled from either the bottom or top of the cavity. Two-dimensional results for the unreinforced matrix and nonclustering particles of relatively small and large particle diameters are shown in cases I to III. Note that the heat transfer coefficient U used in the solidification simulations results in cooling rates and front velocities characteristic of typical casting processes.[81]

All simulations utilize SiC particles and an initial liquid concentration of C_0 = Al-7 wt pct Si, which is thought to reasonably approximate the commonly used A356 commercial alloy whose main alloying elements are Si (7.11 wt pct) and Mg (0.4 wt pct).[82] The initial temperature T_0 is taken as 933.2 and 993.2 K for the sedimentation (cases S1 to S3) and solidification (cases C1 to C4 and I to III) simulations, respectively. The maximum particle fraction ε_{pm} is taken as the random packing fraction (0.637) with the exception of case S1, where it is taken as 0.5. Liquid density and expansion coefficient values shown in Table IV (utilized in the two-dimensional simulations) have been interpolated from the data of Glauner *et al.*[83] Note that the particle thermal conductivity k_p is taken as the low-purity value, which may overestimate the local solidification time as discussed in Hanumanth and Irons.[35]

A. *One-Dimensional Sedimentation*

One-dimensional results for sedimentation in nonclustering (case S1) and clustering (cases S2 and S3) particle systems are shown in Figure 5. No solidification occurs in this

Table IV. Thermophysical Properties and Empirical Constants for an Al-7 Wt Pct Si/SiC System

Quantity	Symbol	Value	Units	Reference
Density	$\rho_l = \rho_l^{\text{ref}}$	2430	kg/m^3	Glauner *et al.*[83]
	ρ_s	2430	kg/m^3	(assumed equal to ρ_l)
	ρ_p	3200	kg/m^3	Smithells[85]
Expansion coefficient	β_T	1.2×10^{-4}	K^{-1}	Glauner *et al.*[83]
	β_C	-2.6×10^{-3}	wt pct Si^{-1}	Glauner *et al.*[83]
Liquid viscosity	μ_l	1.26×10^{-3}	kg/m s	Landolt and Börnstein[86]
Thermal conductivity	k_l	90	W/m K	Thévoz *et al.*[87]
	k_s	159	W/m K	Landolt and Börnstein[86]
	k_p	16	W/m K	Stefanescu *et al.*[28]
Specific heat	c_l	1080	J/kg K	Thévoz *et al.*[87]
	c_s	879	J/kg K	Landolt and Börnstein[86]
	c_p	840	J/kg K	Smithells[85]
Solutal diffusivity	D_l	3×10^{-9}	m^2/s	Rappaz and Thévoz[88]
	D_s	1×10^{-12}	m^2/s	Landolt and Börnstein[89]
Latent heat of fusion (pure Al)	Δh_M	3.9×10^5	J/kg	Thévoz *et al.*[87]
Melting temperature (pure Al)	T_M	933.4	K	Mondolfo[90]
Eutectic temperature	T_E	850.2	K	Mondolfo[90]
Eutectic concentration	C_E	12.5	wt pct Si	Mondolfo[90]
Liquidus slope	m_l	−6.656	K/wt pct Si	Mondolfo[90]
Partition coefficient	κ	0.132	—	Mondolfo[90]
Permeability constant	K_1	6×10^{-4}	—	with data from Bhat[55]

system, and, hence, the governing equations reduce to the mass- and momentum-conservation equations for the liquid and particle phases in one-dimensional form (note that bulk solid quantities reduce to particle quantities for $\varepsilon_s = 0$). In all cases, an initially uniform distribution of particles (or particle clusters) is allowed to settle under gravity until becoming packed at the cavity bottom.

Figure 5(a) plots the time evolution of the denuded and packed zone interface heights during sedimentation of 90 μm nonclustering particles of initial volume fraction 0.20 (case S1). The upper curve in the figure represents the position of the denuded zone interface, while the lower curve represents the position of the packed zone interface. Because the particle density is greater than that of the surrounding liquid, the particles settle downward, which has the effect of decreasing the particle fraction in the upper control volumes while increasing the particle fraction in the lower control volumes. Due to mass conservation, the liquid melt is displaced upward. As the particle fraction increases, the particle viscosity μ_p increases until it becomes infinitely large at the packing point (*i.e.*, $\varepsilon_p \rightarrow \varepsilon_{pm}$). This has the effect of forcing the particle velocity to that of the adjacent control volume (*i.e.*, the wall at zero velocity), such that the particle velocity in each successive packed control volume becomes that of the wall. The experimental data of Hanumanth *et al.*[18] included in the figure were taken from electrical resistance probe measurements at three locations in the casting. The data bands at each location indicate the times required for a 50 pct change in the particle volume fraction and correspond to the interface between the denuded and initial particle fraction zones. Good agreement is seen between the experimental data and the present predictions.

Hanumanth *et al.*[18] also present a model for one-dimensional particle settling, but use the Richardson–Zaki hindered-settling function (Eq. [9]) instead of the Happel relation (Eq. [10]). Preliminary simulations[74] showed that if the Richardson–Zaki relation is used in the present model, the predicted settling rate is about twice as high as with the Happel relation. Hanumanth *et al.* nonetheless show reasonable agreement with the experimental data, which can only be attributed to their use of a liquid melt viscosity that is about 70 pct higher than the one used in the present study (Table IV). Because the present melt viscosity was properly evaluated at the melt temperature,[86] it can be concluded that the Happel relation provides significantly more realistic predictions than the Richardson–Zaki relation. The fact that the latter relation overestimates the settling rates was also found in the recent study by Hanumanth and Irons.[35]

Figures 5(b) and (c) plot the time evolution of the denuded and packed zone interface heights during sedimentation of particle clusters of initial concentration 0.05 (case S2) and 0.15 (case S3), respectively. In either case, particles of diameter $d_p = 14$ μm are assumed to form clusters of diameter $d_c = 38$ μm and an internal particle fraction $\varepsilon_{pi} = 0.42$.[19] The governing equations are identical to those for nonclustering particles, except that the particle fraction ε_p is taken as the cluster fraction $\varepsilon_c = \varepsilon_p/\varepsilon_{pi}$ and the particle density is taken as ρ_c (Table II). Included in the figures are the resistance probe measurements taken by Irons and Owusu–Boahen.[19] As in case S1, the particle clusters settle downward until μ_c becomes infinitely large at the packing point, although in this case packing corresponds to the packing of clusters. Based on the random packing fraction of $\varepsilon_{cm} = 0.637$, the actual particle packing fraction is then $\varepsilon_{pm} = \varepsilon_{pi}\varepsilon_{cm} = 0.27$, which is in agreement with experiments.[14,15,16] Again, good agreement between experiment and theory is found in Figures 5(b) and (c).

B. *One-Dimensional Composite Solidification*

Results are presented in this section for one-dimensional composite solidification (Figure 4(a)) in clustering and nonclustering particle systems (cases C1 to C4). The full set of governing equations is utilized, but in a one-dimensional form. Thermosolutal melt convection is not included, and

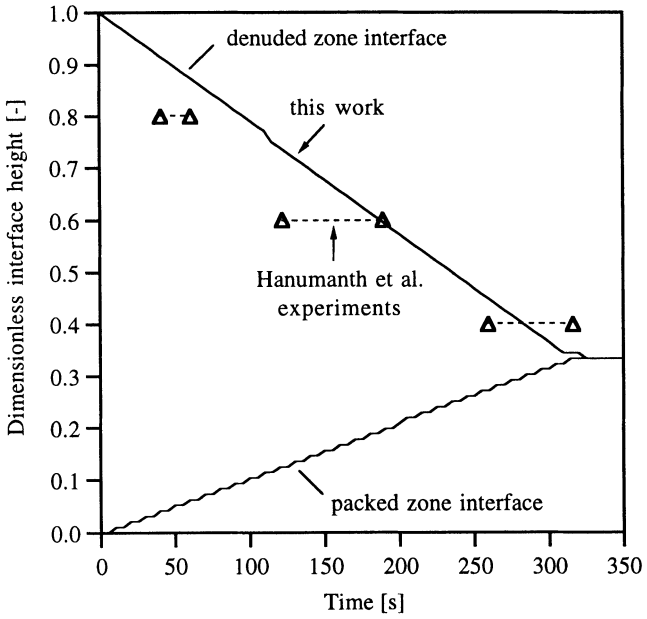

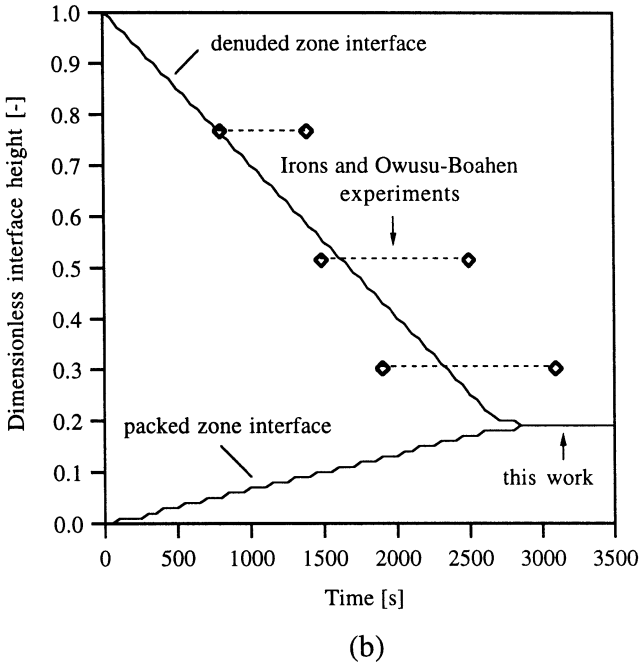

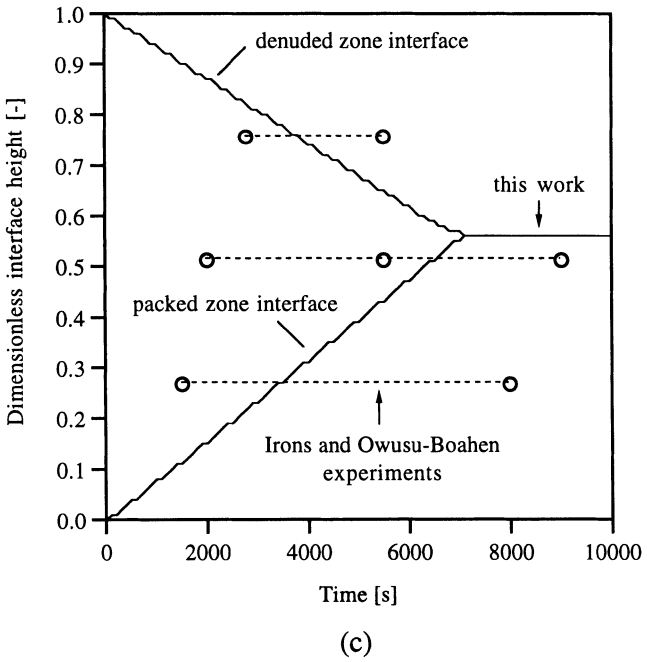

Fig. 5—Comparison of predicted denuded and packed zone interface heights to sedimentation experiments of Hanumanth *et al.*[18] and Irons and Owusu-Boahen:[19] (*a*) $\varepsilon_{po} = 0.20$ nonclustering particles (case S1); (*b*) $\varepsilon_{po} = 0.05$ (case S2); and (*c*) $\varepsilon_{po} = 0.15$ (case S3) clustering particles.

the particles (or particle clusters) simply settle under gravity until becoming packed at the cavity bottom or entrapped by the advancing mush. The bottom-cooled configuration (cases C1 and C2) is similar to the experiments performed by Hanumanth and Irons,[35] who also present a one-dimensional model. Under one-dimensional conditions, the present model can be shown to approximately reduce to their model, with the main exception of the hindered-settling function used (Section II). Hanumanth and Irons[35] report good agreement between their model and measured heat transfer and particle distribution data, which also validates the present model. As already mentioned, however, they found it necessary to use a much higher thermal conductivity of the SiC particles than the one employed here (Table IV), and such an adjustment is recommended for future simulations. The results presented here are intended to illustrate some of the intricate interplays possible between particle settling and entrapment in a simple one-dimensional system.

In all cases, particles of diameter $d_p = 14$ μm are assumed to form clusters (cases C1 and C3) of diameter $d_c = 38$ μm and an internal particle fraction $\varepsilon_{pi} = 0.42$,[19] or remain as individual particles (cases C2 and C4). Further, all simulations utilize a single initial particle concentration, namely, $\varepsilon_{po} = 0.05$. The motivation behind this selection can be seen in Figure 6, which compares the steady-state relative velocities of clustering and nonclustering SiC particles in an Al-7 wt pct Si matrix as a function of particle concentration. The relative velocity is calculated from Eqs. [6] and [7] as

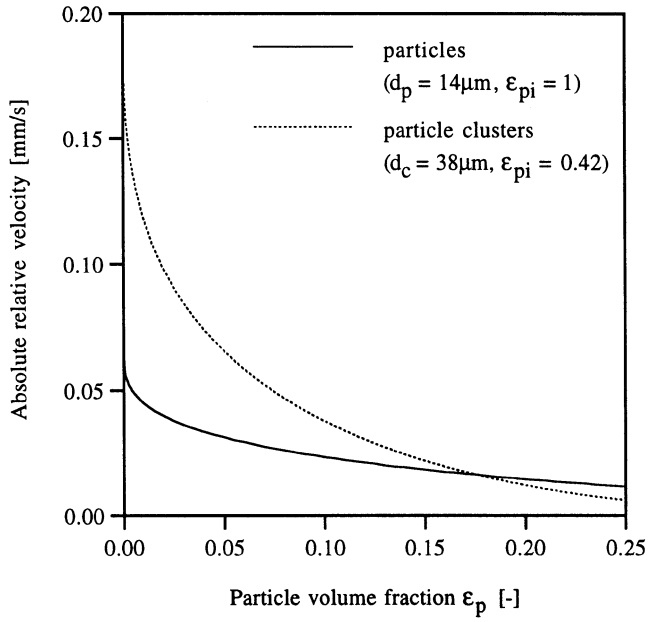

Fig. 6—Steady-state absolute relative velocity between the liquid and particles or particle clusters in an Al-7 wt pct Si/SiC system (Eq. [24]).

$$\mathbf{v}_c - \mathbf{v}_l = \frac{d_c^2 (\rho_l - \rho_c)\, g}{18\ \mu_l \varepsilon_l} f(\varepsilon_l) \qquad [24]$$

where $f(\varepsilon_l)$ is the hindered-settling function given by the Happel model and ρ_c is the cluster (or particle) density based on ε_{pi}. As can be seen in the figure, the maximum relative velocity is obtained as the particle concentration goes to zero. Hence, $\varepsilon_{po} = 0.05$ is expected to produce a significant difference in the amount of settling between clustering and nonclustering particles. It is interesting to note that the relative velocity of the cluster system becomes smaller than that of the nonclustering system at $\varepsilon_p > 0.18$, at which point significant liquid-particle interactions occur in the clustering system which serve to lower the relative velocity below that of the nonclustering system.

Simulation results for the denuded and packed zone interface heights and liquidus, and eutectic isotherm positions for both bottom- and top-cooled configurations, are shown in Figure 7. For the bottom-cooled cases C1 and C2 (Figures 7(a) and (b)), virtually no particle packing is observed near the cavity bottom, since the particles have very little time to accumulate before solidification (and entrapment) occurs in this region. On the other hand, a large amount of particle settling is observed near the top of the cavity, since the mush reaches this region last. Opposite trends are observed in the top cooled cases C3 and C4 (Figures 7(c) and (d)), where packing occurs near the cavity bottom and very little denuded zone formation occurs near the top. Again, this is due to the solidification direction, which has the effect of freezing the particles near the cooled wall before they can settle significantly, but allows significant settling in the region opposite the cooled wall. It is observed in both bottom and top cooled cases that a higher degree of settling occurs in the cluster systems (cases C1 and C3; Figures 7(a) and (c)), which is evidenced by the larger denuded and packed zones. This is due to the smaller drag force exerted on the larger particle clusters, which results in a larger particle-liquid relative velocity and, hence, more settling prior to particle entrapment. Finally, results[74] (not shown here) for the species macrosegregation indicate that the melt velocities are too small in the one-dimensional cases to cause much variation in the Si concentration over the height of the solidified ingot.

C. *Two-Dimensional Composite Solidification*

Two-dimensional results for composite solidification in a cavity cooled from one side (Figure 4(b)) are shown in the following figures, including results for an unreinforced matrix (case I) which is intended to serve as a base case, as well as two reinforced cases utilizing relatively small (case II) and large (case III) particle diameters. Thermosolutal melt convection and particle transport/settling are both included in the simulations. Results are presented in plots of bulk solid fraction (ε_b) and liquid velocity ($\mathbf{v}_l$), Figures 8 through 10; solid fraction (ε_s) and liquid-solid relative velocity ($\mathbf{v}_l - \mathbf{v}_s$), Figures 11 and 12; particle fraction (ε_p) and particle-liquid relative velocity ($\mathbf{v}_p - \mathbf{v}_l$), Figures 13 through 15. Isotherms (Figures 16 and 17) and mixture concentration (Figure 18) are presented at various times, as well as plots of final particle fraction, mixture concentration, and eutectic fraction (Figures 19, 20 and 21, respectively). The mixture concentration C_m is defined as

$$C_m = \frac{\varepsilon_l \rho_l C_l + \varepsilon_s \rho_s C_s}{\varepsilon_l \rho_l + \varepsilon_s \rho_s} \qquad [25]$$

Dimensionless x and y coordinates $X = x/L$ and $Y = y/H$ are used to identify specific regions on the figures. Note that velocity vectors are plotted on a slightly coarser grid in order to more easily view the results.

1. *Unreinforced matrix (case I)*

The bulk solid (*i.e.*, solid in this case) fraction and liquid velocity at $t = 50$ seconds for the unreinforced matrix (case I) are plotted in Figure 8(a). Due to cooling at the west wall of the cavity, the liquid density in this region increases and the liquid flows downward, causing an essentially single counterclockwise convective cell to form, although some recirculation is observed near corners. No solid has formed in the cavity at this time since the temperature everywhere is above the initial liquidus temperature of $T_{lq}(C_0) = 886.8$ K. At $t = 100$ seconds (Figure 9(a)), solid has formed at the west wall and the mush has advanced into the cavity. As seen in this plot and the liquid-solid relative velocity plot of Figure 11(a), the liquid velocity is relatively small in the mush due to the increased interfacial drag in this region. The nonvertical nature of the solidification front is due in part to thermal buoyancy forces which cause a bowing of the isotherms (Figure 16(a)). During solidification, however, solutal buoyancy forces also come into play, due to the rejection of Si in this system caused by the smaller solubility of Si in the solid than in the liquid. The mushy region becomes depleted of solute in this case (*i.e.*, becomes negatively segregated), whereas the liquid becomes enriched. Because the rejected solute is heavier than the bulk liquid (*i.e.*, $\beta_C < 0$), solutal buoyancy forces cause it to flow downward and become deposited at the bottom of the cavity. The increase in solute results in a depression of the liquidus temperature, and accounts for the fully liquid region observed in the lower right corner of the cavity where $T < T_{lq}(C_0)$.

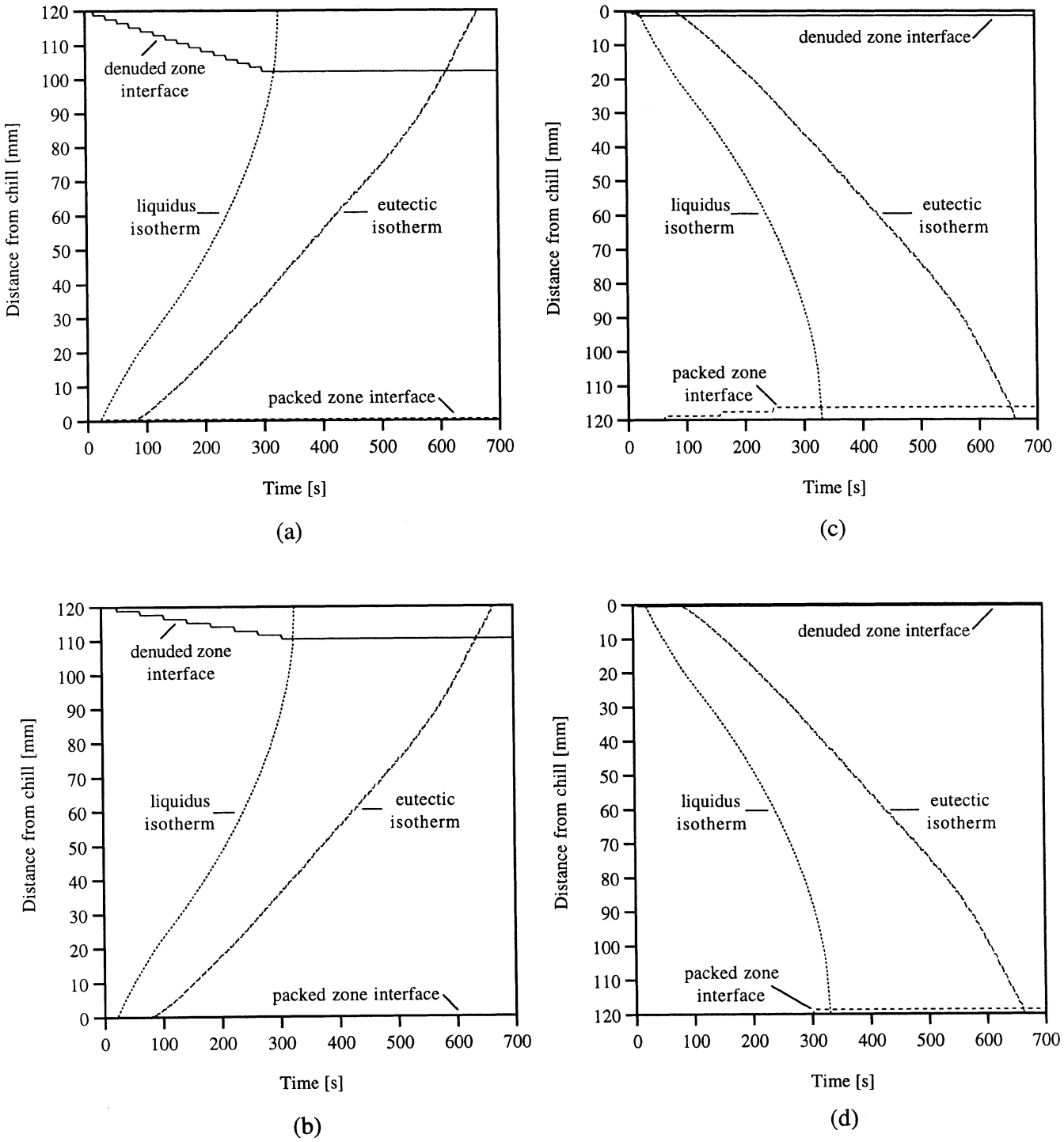

Fig. 7—One-dimensional composite solidification results: (*a*) clustering (case C1) and (*b*) nonclustering (case C2) particle systems with bottom cooling; (*c*) clustering (case C3); and (*d*) nonclustering (case C4) particle systems with top cooling.

At $t = 150$ seconds, the mush has advanced into the majority of the cavity, as shown in Figures 10(a) and 12(a). The liquid velocities near the west wall have become very small at this point due to the ever-increasing interfacial drag caused by the relatively impermeable mush, whereas the liquid velocities near the east wall are larger since the mush is more permeable in this region. A fully liquid region is observed near the bottom right corner and east wall of the cavity, which is due to the rejected solute transported to this region which lowers the local liquidus temperature. This behavior can be seen in the isotherm and mixture concentration plots of Figures 17(a) and 18(a), respectively, where the region of positive segregation in the right-hand portion of the cavity has lowered the liquidus below that of $T_{liq}(C_0)$. Solidification tends to be delayed or accelerated where the mixture concentration is relatively high or low, respectively, such as those regions near the bottom or top of the cavity, as shown in Figure 12(a). Interestingly, relatively large liquid velocities are observed near an irregularly shaped 0.1 solid fraction contour at approximately Y

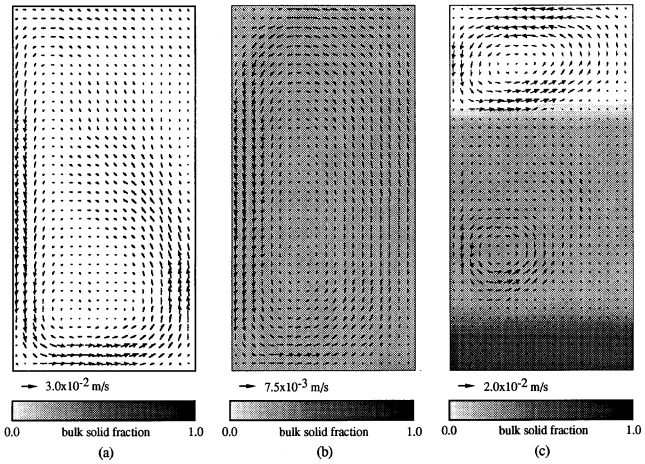

Fig. 8—Bulk solid fraction and liquid velocity at $t = 50$ s: (*a*) case I (unreinforced), (*b*) case II (small particles), and (*c*) case III (large particles).

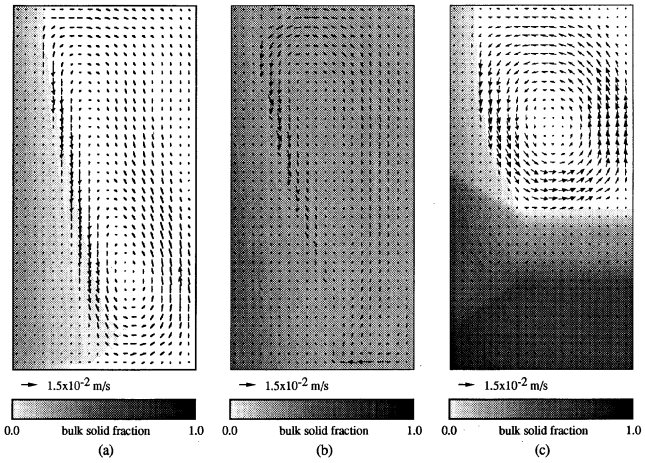

Fig. 9—Bulk solid fraction and liquid velocity at $t = 100$ s: (*a*) case I (unreinforced), (*b*) case II (small particles), and (*c*) case III (large particles).

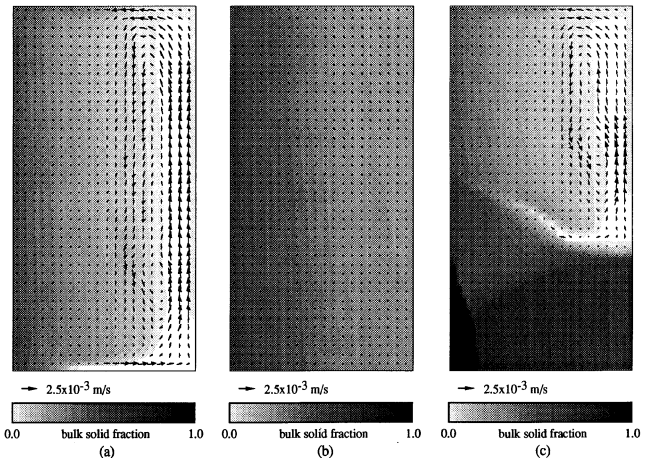

Fig. 10—Bulk solid fraction and liquid velocity at $t = 150$ s: (*a*) case I (unreinforced), (*b*) case II (small particles), and (*c*) case III (large particles).

$= 0.25$. This is evidence that a preferred channel may be forming due to the rejection of solute-rich fluid, which may delay solidification and/or even cause partial remelting in this region. Such solute-rich channels appear as ''fingers'' in the mixture concentration plot. Accelerated solidification is also observed near the east wall, which is essentially separated from the mush in the cavity interior. Such isolated ''islands'' of solid have also been observed by Schneider and Beckermann[79] and are attributed to a combination of temperature and concentration, which has resulted in an elevation of the liquidus.

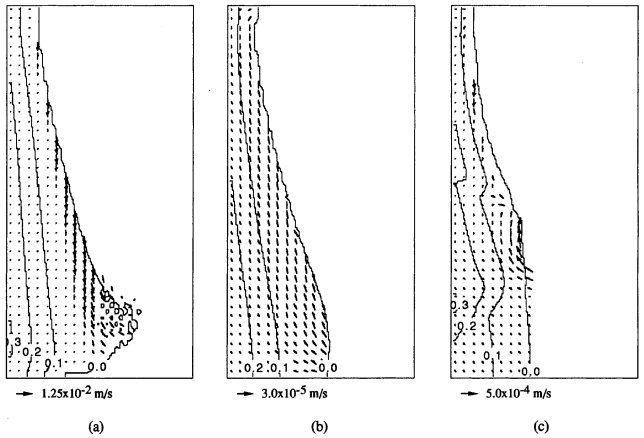

Fig. 11—Solid fraction contours and liquid-solid relative velocity at $t = 100$ s: (*a*) case I (unreinforced), (*b*) case II (small particles), and (*c*) case III (large particles).

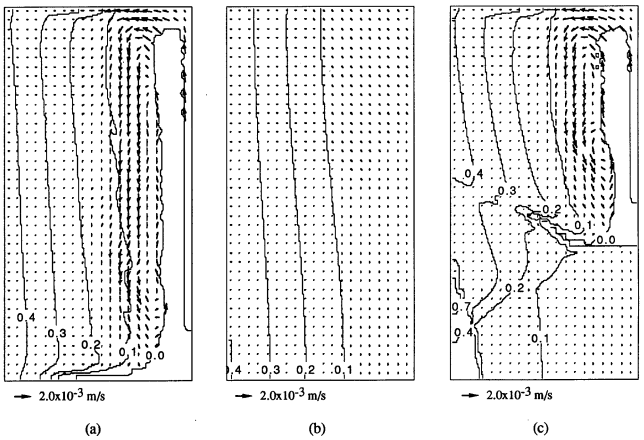

Fig. 12—Solid fraction contours and liquid-solid relative velocity at $t = 150$ s: (*a*) case I (unreinforced), (*b*) case II (small particles), and (*c*) case III (large particles).

The total solidification time for case I is approximately 470 seconds. Figure 20(a) plots the final mixture concentration. Regions of positive segregation are observed near the bottom and right-hand portions of the cavity due to the transport of relatively dense solute to these last-solidifying regions. Conversely, regions of negative segregation are observed near the top and left portions of the cavity where the solute has been transported out. Several of the aforementioned channel segregates are seen to exist where the mixture concentration is higher than that in the immediate neighborhood (*e.g.*, $X = 0.66$ and $Y = 0.25$). Interestingly, regions of negative segregation are seen to exist near these channels, which is likely due to the feeding of solute to the channels. Similar behavior was observed by Wang and Beckermann[78] in Al-Cu systems (where β_c is also negative) with identical boundary conditions, although macro-

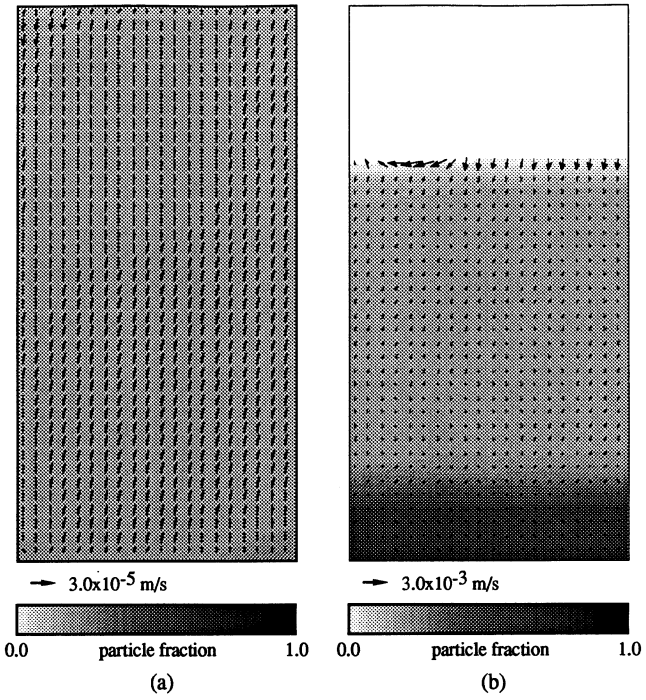

Fig. 13—Particle fraction and particle-liquid relative velocity at $t = 50$ s: (*a*) case II (small particles) and (*b*) case III (large particles).

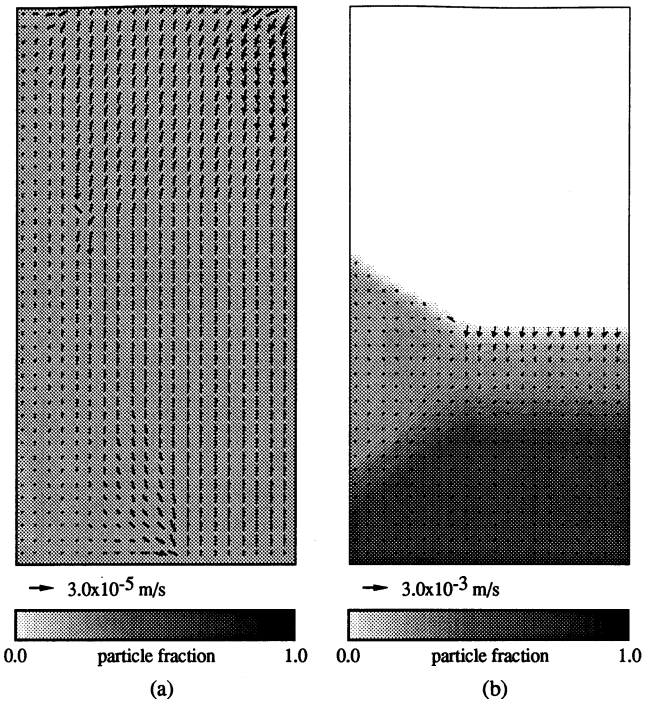

Fig. 14—Particle fraction and particle-liquid relative velocity at $t = 100$ s: (*a*) case II (small particles) and (*b*) case III (large particles).

segregation is not as pronounced in the current system since the solutal buoyancy forces are weaker than those for Al-Cu. The eutectic fraction plotted in Figure 21(a) tends to mirror that of the mixture concentration, with more eutectic formed where positive segregation is largest. This is consistent with the observations of Schneider and Beckermann.[79] The Scheil model liquid fraction may be calculated as[81]

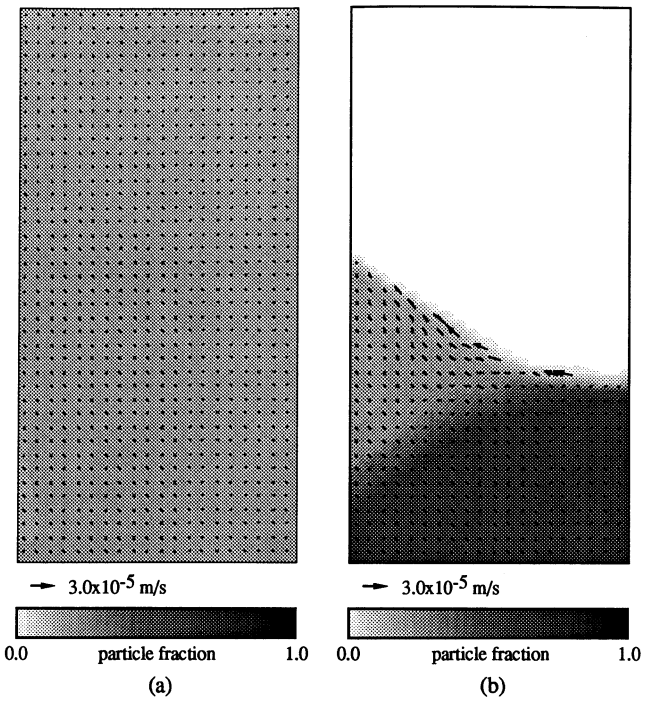

Fig. 15—Particle fraction and particle-liquid relative velocity at $t = 150$ s: (*a*) case II (small particles) and (*b*) case III (large particles).

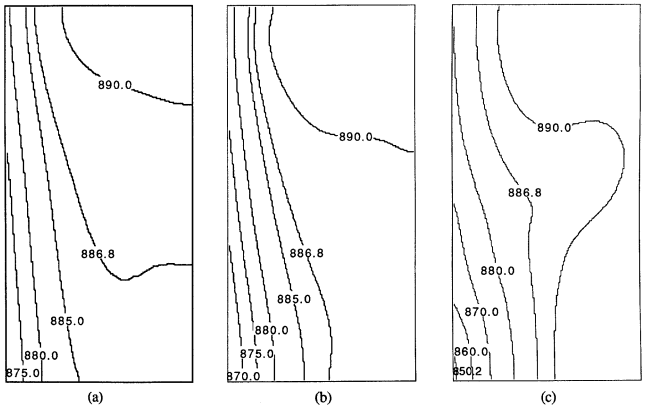

Fig. 16—Isotherms (*K*) at $t = 100$ s: (*a*) case I (unreinforced), (*b*) case II (small particles), and (*c*) case III (large particles).

$$\varepsilon_l = \left(\frac{C_l}{C_0}\right)^{\frac{1}{\kappa-1}} \qquad [26]$$

The Scheil eutectic fraction obtained from Eq. [26] for the unreinforced system is equal to 0.51. It can be seen that the predicted eutectic fraction is near the Scheil value in some portions of the cavity, which suggests that macrosegregation and backdiffusion is of minor importance at those locations. However, large differences between the predicted and Scheil eutectic fractions exist in regions where significant macrosegregation has occurred.

2. *Reinforced matrix with small particles (case II)*

Figure 8(b) plots the bulk solid (*i.e.*, solid plus particle) fraction and liquid velocity at $t = 50$ seconds for the reinforced matrix with relatively small particles (case II). At this time, a small portion of solid has formed in the bottom left corner of the cavity, but this is not apparent from the

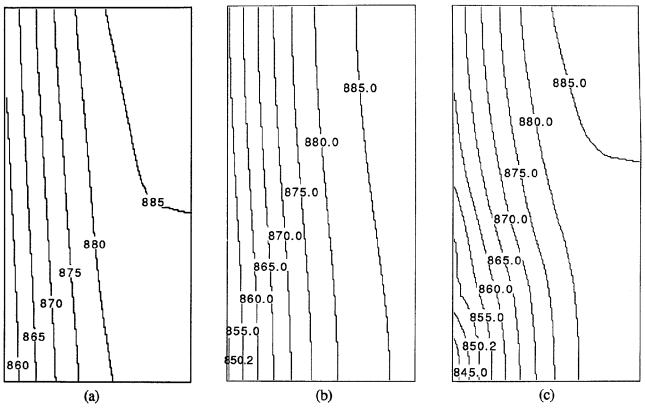

Fig. 17—Isotherms (K) at $t = 150$ s: (a) case I (unreinforced), (b) case II (small particles), and (c) case III (large particles).

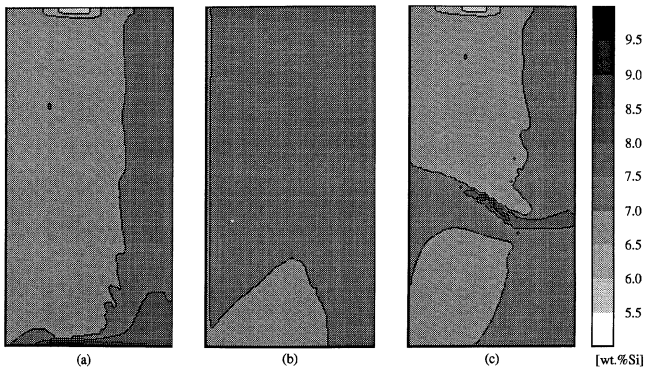

Fig. 18—Mixture concentration at $t = 150$ s: (a) case I (unreinforced), (b) case II (small particles), and (c) case III (large particles).

figure. What is apparent is that the liquid velocity is roughly 4 times smaller than that of the unreinforced case (Figure 8(a)) due to the increased viscosity brought about by the particle phase. The particle-liquid relative velocity shown in Figure 13(a) is small due to the relatively small particles used in this simulation (*i.e.*, large particle-liquid drag), and as a result the particles closely follow the motion of the liquid. Negligible particle settling has occurred at this time, and hence, the particle fraction is approximately equal to the initial particle fraction $\varepsilon_{po} = 0.20$ throughout the domain. Note that particles are assumed to become immediately entrapped (*i.e.*, $\mathbf{v}_p \rightarrow 0$) once the local solid fraction becomes greater than zero.

At $t = 100$ seconds, the liquid velocity (Figure 9(b)) is comparable to that of the unreinforced case shown in Figure 9(a), and results from previous times for case II (not shown) indicate that the liquid velocity steadily increases up until approximately this point. From Figure 11(b), it is seen that the liquid velocity in the mush is substantially lower than that for the unreinforced case and has switched direction from the negative to the positive y direction, which is in contradiction to the thermosolutal buoyancy forces in this region. The liquid in the mush travels in the positive y direction, because the liquid displaced by particle settling can more easily flow back up through the mush than enter the main circulation cell in the liquid-particle zone. From Figure 14(a), it is seen that negligible particle settling occurs before the particles become entrapped, and that the particle-liquid relative velocity becomes the negative of the

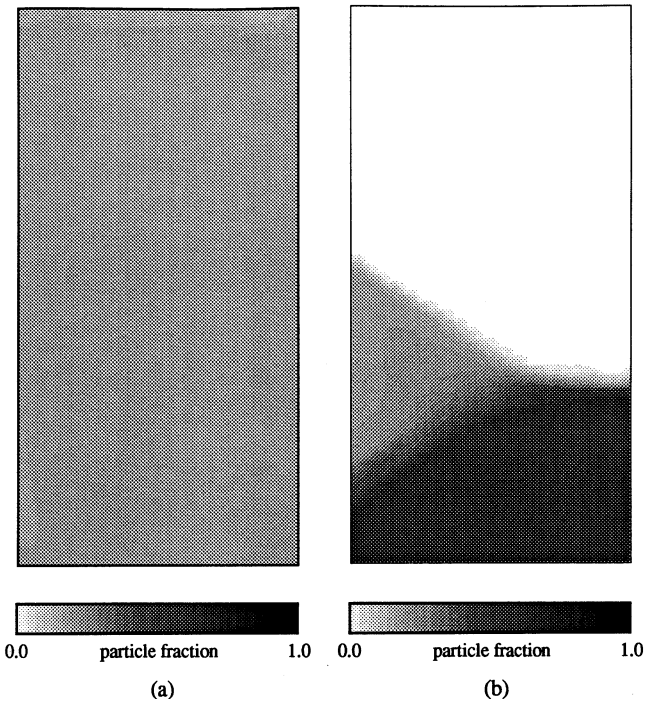

Fig. 19—Final particle fraction: (a) case II (small particles) and (b) case III (large particles).

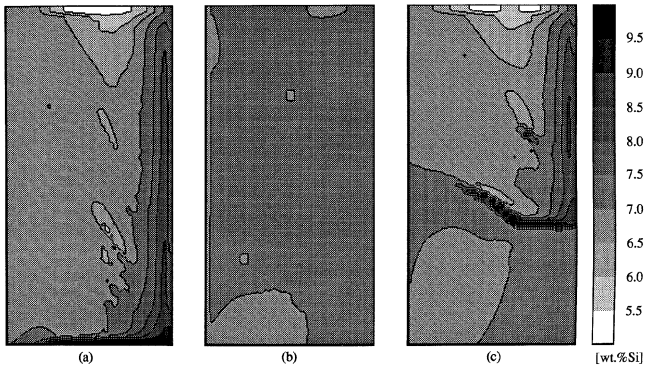

Fig. 20—Final mixture concentration: (a) case I (unreinforced), (b) case II (small particles), and (c) case III (large particles).

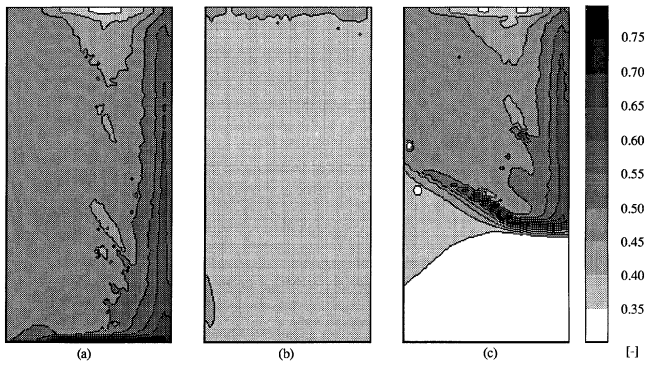

Fig. 21—Eutectic fraction: (a) case I (unreinforced), (b) case II (small particles), and (c) case III (large particles).

liquid velocity in the mush-particle region where the particle velocity is forced to zero. Further, the initial liquidus isotherm essentially corresponds to the mushy zone inter-

face, as shown in Figure 16(b), implying that very little macrosegregation is occurring in the system. However, slightly lower temperatures are observed in the lower left corner, which suggests that solidification is occurring more rapidly in the reinforced case.

At $t = 150$ seconds, the mush has advanced into the entire cavity and, hence, all of the particles have become macroscopically frozen. As shown in Figures 10(b) and 12(b), the liquid has once again reverted to a single counterclockwise cell, although the large interfacial drag brought about by the mush and stationary particles has resulted in very small liquid velocities ($\sim$1 μm/s). Once again it is noted that very little particle settling occurs prior to particle entrapment (Figure 15(a)). As a result of the very small liquid velocities, the isotherms in Figure 17(b) are relatively straight, which is indicative of diffusion-dominated solidification. It is noted in this plot, however, that a small amount of eutectic fraction has formed in the bottom left corner of the cavity where the temperature is equal to $T_E = 850.2$ K. No eutectic fraction was observed at this time in the unreinforced case (Figure 17(a)). Hence, solidification proceeds more rapidly in the reinforced case, which is due to the smaller amount of phase-change material (*i.e.*, liquid) in the system. Some macrosegregation has occurred very near the west wall and in the bottom left corner, as shown in Figure 18(b), but the amount is very small.

The total solidification time for case II is approximately 410 seconds, which as expected is lower than that for the unreinforced case. The final particle fraction shown in Figure 19(a) is essentially that of the initial value of $\varepsilon_{po} = 0.20$ since the particles were entrapped before they could significantly settle. The final mixture concentration plotted in Figure 20(b) is also essentially that of the initial value of $C_0 = 7$ wt pct Si due to the very small liquid velocities caused by the large interfacial drag. As a result, no channel segregates are observed to occur in this case. It is interesting to note that the eutectic fraction shown in Figure 21(b) is approximately equal to 0.4 throughout, which is lower than that for the reinforced case. This is again due to the presence of the reinforcement, which reduces the amount of phase-change volume available. The Scheil equation in the presence of a stationary particle phase may be derived in a manner similar to that in Feller and Beckermann,[84] in which the liquid and solid species equations are combined (under steady-state conditions with no convective or diffusive terms) and integrated to obtain

$$\varepsilon_l(\varepsilon_p) = (1 - \varepsilon_p) \left(\frac{C_l}{C_0}\right)^{\frac{1}{\kappa - 1}} \qquad [27]$$

where the liquid fraction at $\varepsilon_s = 0$ is equal to $(1 - \varepsilon_p)$. For $\varepsilon_p = 0.20$, the eutectic fraction is equal to 0.41, which is very close to that obtained in the simulation. Hence, Scheil behavior is approached in this system due to an essentially constant particle concentration, negligible macrosegregation, and negligible backdiffusion.

3. *Reinforced matrix with large particles (case III)*

The bulk solid fraction and liquid velocity at $t = 50$ seconds for the reinforced matrix with relatively large particles (case III) are plotted in Figure 8(c). Corresponding results for the particle fraction and particle-liquid relative velocity are shown in Figure 13(b). It is apparent that a large amount of particle settling has occurred at this time, as evidenced by the relatively large denuded and packed zones existing in the upper and lower portions of the cavity, respectively. Such dramatic particle settling is due to the large particles used in this simulation, which result in a smaller particle-liquid interfacial drag and, hence, a larger particle-liquid relative velocity. Interestingly, separate convective cells have formed in the denuded and initial particle fraction zones (Figure 8(c)), which is due to the differing interfacial drag in the respective regions. Note that the particle-liquid relative velocity is largest at the interface between the denuded and initial particle fraction regions where the particles are less hindered. Again, a small amount of solid has formed at this time in the bottom left corner of the cavity, but this is not apparent from the figures. Recall that particle entrapment is again assumed to occur when the local solid fraction becomes larger than zero.

At $t = 100$ seconds, a large denuded region has formed which contains an essentially single counterclockwise convective cell, as shown in Figure 9(c). The solid and particle fractions at this time are shown in Figures 11(c) and 14(b), respectively. While both the denuded and packed zones have increased in size, it is seen that the advancing mush has inhibited the growth of these zones along the west wall. It is interesting to note in Figure 11(c) that the liquid velocity goes downward through the mush in the upper half of the cavity (where there are no particles), whereas it goes upward through the mush and stationary particles in the bottom half of the cavity. The downward flow in the upper half is due to thermal and solutal buoyancy forces (as in case I), whereas the upward flow in the lower half is due to the displacement of liquid caused by particle settling (as in case II). The initial liquidus isotherm (Figure 16(c)) corresponds to the mushy zone interface in the lower half of the cavity, whereas some deviation is observed in the unreinforced upper half where macrosegregation is more pronounced. A small amount of eutectic fraction has formed in the bottom left corner of the cavity due to the large volume of particles in this region and, hence, a smaller amount of phase-change material.

At $t = 150$ seconds, all of the particles have reached packing or have become entrapped by the growing mush. It is observed in Figure 10(c) that the unreinforced zone in the upper half of the cavity exhibits flow behavior similar to that of case I, where the interface between the particle bed and fully liquid region has effectively become the cavity bottom. The liquid velocities in the mush-particle zone (Figure 15(b)) are very small due to the large interfacial drag exerted on the liquid, although the particle-liquid relative velocities are larger than in case II since larger particles have a smaller drag force. As in case I, a fully liquid region is observed where macrosegregation of solute has caused a depression of the liquidus (*e.g.*, near the east side and above the particle bed), as can be deduced from the isotherm and mixture concentration plots of Figures 17(c) and 18(c), respectively. However, a relatively large amount of eutectic fraction has formed at this time near the bottom left corner due to the relatively large particle fraction in this region. Note the fully solid and particle regions (*i.e.*, $\varepsilon_b \rightarrow 1$) in this region, as shown in Figure 10(c). This figure and the solid contour plot of Figure 12(c) show relatively large liquid

velocities at roughly $X = 0.66$ and $Y = 0.66$, indicating the formation of channel segregates as observed in case I.

The total solidification time for case III is approximately 440 seconds, which is between that obtained in cases I and II. The final particle fraction plot of Figure 19(b) shows the large denuded and packed zones formed in this case as well as a region of particles at roughly the initial particle concentration that became entrapped before they could settle further. The result is the formation of ramps at the left side of each zone. The final mixture concentration plot of Figure 20(c) shows a combination of the macrosegregation phenomena observed in the previous two cases. This is due to the stratification of particles resulting in very different macrosegregation behavior. In the upper unreinforced region (*i.e.*, analogous to case I), a large region of positive segregation is observed in the middle right portion of the cavity where relatively dense solute has been transported in, whereas a region of negative segregation is observed in the upper part of the cavity where solute has been transported out. The continued formation of channel segregates is observed at approximately $X = 0.66$ and $Y = 0.66$, as well as at a feeding region adjacent to the channels. Very little macrosegregation is observed in the reinforced portion of the cavity due to the large drag exerted on the liquid (as in case II). As for the unreinforced case, the eutectic fraction shown in Figure 21(c) mirrors the mixture concentration in the upper half of the cavity where no particles are present. In the reinforced region, however, the eutectic fraction is scaled by the volume of particles present, *i.e.*, the eutectic fraction is lowest where the volume fraction of particles is the largest (*i.e.*, in the packed zone). As for case II, Scheil-type behavior is approached in the reinforced region due to negligible macrosegregation and backdiffusion. For example, the predicted Scheil (*i.e.*, Eq. [27]) and simulation eutectic fractions at a particle concentration of 0.30 are 0.36 and 0.35, respectively.

V. CONCLUSIONS

A multiphase model for MMPC solidification has been developed and applied to sedimentation and solidification in various one- and two-dimensional Al-7 wt pct Si/SiC systems. Good agreement is found between simulation and available experimental sedimentation results in A356 systems containing nonclustering and clustering particle systems. One-dimensional composite solidification results illustrate the effect of particle clustering and cooling direction on the final macroscopic particle distribution, with the greatest concentration of particles found to occur near the wall opposite the chill. Two-dimensional simulations examine macroscopic particle transport as well as its effect on buoyancy-driven melt flow, macrosegregation, and eutectic formation. For the unreinforced alloy, macrosegregation is widespread with several channel segregates formed due to thermosolutal convection within the mush. For the reinforced alloy with small particles, very little particle settling prior to entrapment is observed since the drag is relatively high (*i.e.*, the particles closely follow the motion of the liquid). In contrast, large particles result in a large amount of settling and packing prior to entrapment due to the smaller drag and relatively large particle-liquid relative velocity.

In the presence of particles, convection during solidification is found to be substantially reduced due to the relatively large interfacial drag exerted on the liquid by the stationary mush and particles, which effectively acts to decrease the permeability of the mush, as well as due to the increased viscosity in the liquid-particle zone. As a result, macrosegregation is negligible where reinforcement is present, and solidification behavior approaches that predicted by the Scheil model. This results in a combination of the previous-case behavior for the large particle case due to the formation of two distinct zones where particles are absent and present, respectively. Buoyancy-driven convection in the melt is generally significant, and consideration of settling alone is not sufficient since particle motion occurs due to melt convection. It is pointed out that the present model enables the prediction of the particle and melt velocities at the front, which are primary ingredients in any particle rejection model that accounts for flow.

Future work includes investigation of a number of phenomena, including:

1. particle rejection at a relatively dense mush/liquid interface in the presence of flow;
2. macroscopic particle movement within a relatively open mushy zone;
3. the effect of a nonstationary solid phase;
4. non-Newtonian flow behavior; and
5. microstructural changes and transitions due to interactions between the matrix and reinforcement.

More solidification experiments (over a larger range of cooling rates) are required before many of these issues can be addressed. With concurrent experiments, the present model can provide a general framework to investigate more advanced phenomena related to the solidification of MMPCs.

NOMENCLATURE

C	concentration of Si (wt pct)
C_D	drag coefficient (—)
c	specific heat (J/kg K)
D	mass diffusivity (m^2/s)
$\tilde{D}$	interfacial species exchange coefficient (kg/m^3 s)
d	diameter (m)
f	hindered settling function (—)
g	acceleration due to gravity (m/s^2)
H	cavity height (m)
K	permeability (m^2)
K_1	permeability constant (—)
k	thermal conductivity (W/m K)
L	cavity length (m)
l	diffusion length (m)
m	phase diagram slope (K/wt pct)
n	coordinate normal to the wall (m)
P	hydrodynamic pressure (N/m^2)
Re	Reynolds number (—)
S	interfacial area concentration (m^{-1})
T	temperature (K)
t	time (s)
U	heat-transfer coefficient (W/m^2 K)
V	velocity (m/s)
$\mathbf{v}$	velocity vector (m/s)
Y	dimensionless y distance (—)

y vertical coordinate (m)
X dimensionless x distance (—)
x horizontal coordinate (m)

Greek Symbols

β interfacial momentum exchange coefficient (kg/m^3 s)
β_T thermal expansion coefficient (K^{-1})
β_C solutal expansion coefficient (wt pct^{-1})
ε volume fraction (—)
κ partition coefficient (—)
λ spacing (m)
η parameter in drag model (—)
μ dynamic viscosity (kg/m s)
ρ density (kg/m^3)
Ψ field quantity
Δh latent heat of fusion (J/kg)

Subscripts

a ambient
b bulk solid phase
C concentration
c cluster
cr critical
E eutectic point
k phase k
kj pertinent to phase k at the k/j interface
l liquid phase
lc liquid within cluster
lq liquidus
M melting point of pure substance
m mixture
0 initial
p particle phase
pi internal particle
pm maximum particle
s solid phase
T temperature
1 primary
2 secondary
∞ infinite domain

Superscripts

ref reference
— average over the interfacial area

ACKNOWLEDGMENTS

This work was supported by the National Science Foundation under Grant No. CTS-8957149. One of the authors (RJF) is thankful to the Iowa College Student Aid Commission for assistance through a Tuition Grant Award.

REFERENCES

1. P. Rohatgi: *JOM*, 1991, Apr., pp. 10-15.
2. J.E. Allison and G.S. Cole: *JOM*, 1993, Jan., pp. 19-24.
3. P.K. Rohatgi, R. Asthana, and S. Das: *Int. Met. Rev.*, 1986, vol. 31, pp. 115-39.
4. A. Mortensen and I. Jin: *Int. Mater. Rev.*, 1992, vol. 37, pp. 101-28.
5. D.J. Lloyd: *Int Mater. Rev.*, 1994, vol. 39, pp. 1-23.
6. B.P. Krishnan, H.R. Shetty, and P.K. Rohatgi: *Trans. AFS*, 1976, vol. 76, pp. 73-80.
7. D.J. Lloyd: *Metal Matrix Composites—Processing, Microstructure and Properties*, Proc. 12th Risø Int. Symp. on Materials Science, N. Hansen *et al.*, eds., 1991, Risø, Roskilde, Denmark, pp. 81-99.
8. V.J. Michaud: in *Fundamentals of Metal Matrix Composites*, S. Suresh, A. Mortensen, and A. Needlemaned, eds., Butterworth-Heinemann, Stoneham, MA, 1993, pp. 3-22.
9. Q. Han and J.D. Hunt: *J. Cryst. Growth*, 1994, vol. 140, pp. 406-13.
10. Q. Han and J.D. Hunt: *Iron Steel Inst. Jpn. Int.*, 1995, vol. 35, pp. 693-99.
11. R. Asthana and S.N. Tewari: *J. Mater. Sci.*, 1993, vol. 28, pp. 5414-24.
12. G.B. Wallis: *One-Dimensional Two-Phase Flow*, McGraw-Hill, New York, NY, 1969.
13. S.L. Soo: *Multiphase Fluid Dynamics*, Science Press, Beijing, 1990.
14. F.M. Yarandi, P.K. Rohatgi, and S. Ray: *Proc. 2nd Int. Conf. on the Processing of Semi-Solid Alloys and Composites*, S.B. Brown and M.C. Flemings, eds., TMS, Cambridge, MA, 1992, pp. 447-65.
15. P.K. Rohatgi, R. Sathyamoorthy, C.S. Narendranath, and D. Nath: *AFS Trans.*, 1993, vol. 101, pp. 597-604.
16. N. Setargew, B.A. Parker, and M.J. Couper: *Advanced Composites '93*, Int. Conf. on Advanced Composite Materials, T. Chandra and A.K. Khingra, eds., TMS, Warrendale, PA, 1993, pp. 1021-27.
17. D.J. Lloyd and B. Chamberlain: *Cast Reinforced Metal Composites*, ASM INTERNATIONAL Conf. Proc., S.G. Fishman and A.K. Dhingra, eds., ASM INTERNATIONAL, Metals Park, OH, 1988, pp. 263-69.
18. G.S. Hanumanth, G.A. Irons, and S. Lafreniere: *Metall. Trans. B*, 1992, vol. 23B, pp. 753-63.
19. G.A. Irons and K. Owusu-Boahen: *Metall. Mater. Trans. B*, 1995, vol. 26B, pp. 981-89.
20. A.E. Fouda and C.E. Capes: *Agglomeration '81*, O. Molerus and W. Hufnagel, eds., VDI-Gesellschaft Verfahrenstechnik und Chemieingenieurwesen (GVC), Germany, 1981, pp. E34-E50.
21. R. Sasikumar and B.C. Pai: in *Solidification Processing—1987*, H. Jones, ed., The Institute of Metals, London, 1988, pp. 451-53.
22. R. Sasikumar and M. Kumar: *Acta Metall. Mater.*, 1991, vol. 39, pp. 2503-08.
23. R. Sasikumar, T.R. Ramamohan, and B.C. Pai: *Acta Metall. Mater.*, 1989, vol. 37, pp. 2085-91.
24. D.M. Stefanescu and F. Rana: in *Microstructural Development and Control in Materials Processing*, D.R. Durham and A. Saigal, eds., ASME, Fairfield, NJ, 1989, pp. 95-102.
25. D.M. Stefanescu, S. Ahuja, B.K. Dhindaw, and R. Phalnikar: *Proc. 2nd Int. Conf. on the Processing of Semi-Solid Alloys and Composites*, S.B. Brown and M.C. Flemings, eds., TMS, Cambridge, MA, 1992, pp. 406-16.
26. D.M. Stefanescu, A. Moitra, A.S. Kacar, and B.K. Dhindaw: *Metall. Trans. A*, 1990, vol. 21A, pp. 231-39.
27. D. Shangguan, S. Ahuja, and D.M. Stefanescu: *Metall. Trans. A*, 1992, vol. 23A, pp. 669-80.
28. D.M. Stefanescu, B.K. Dhindaw, S.A. Kacar, and A. Moitra: *Metall. Trans. A*, 1988, vol. 19A, pp. 2847-55.
29. X. Guo and D.M. Stefanescu: *AFS Trans.*, 1992, vol. 100, pp. 273-79.
30. D.J. Lloyd: *Compos. Sci. Technol.*, 1989, vol. 35, pp. 159-79.
31. P.K. Rohatgi, F.M. Yarandi, and Y. Liu: *Cast Reinforced Metal Composites*, ASM INTERNATIONAL Conf. Proc., S.G. Fishman and A.K. Dhingra, eds., ASM INTERNATIONAL, Metals Park, OH, 1988, pp. 249-55.
32. P.K. Rohatgi, F.M. Yarandi, Y. Liu, and R. Asthana: *Mater. Sci. Eng. A*, 1991, vol. A147, pp. L1-L6.
33. P.K. Rohatgi, K. Pasciak, C.S. Narendranath, S. Ray, and A. Sachdev: *J. Mater. Sci.*, 1994, vol. 29, pp. 5357-66.
34. C.G. Kang, S. Ray, and P.K. Rohatgi: *Mater. Sci. Eng. A*, 1994, vol. A188, pp. 193-99.
35. G.S. Hanumanth and G.A. Irons: *Metall. Mater. Trans. B*, 1996, vol. 27B, pp. 663-71.
36. D.A. Drew: *Ann. Rev. Fluid. Mech.*, 1983, vol. 15, pp. 261-91.
37. H.P. Greenspan and M. Ungarish: *Int. J. Multiphase Flow*, 1982, vol. 8, pp. 587-604.
38. D. Gidaspow: *Appl. Mech. Rev.*, 1986, vol. 39, pp. 1-23.
39. C. Bailey, M. Cross, and D. Edwards: *Partic. Sci. Technol.*, 1987, vol. 5, pp. 357-70.
40. R.C. Givler and R.R. Mikatarian: *Trans. ASME*, 1987, vol. 109, pp. 324-31.
41. J. Yagi: *Iron Steel Inst. Jpn. Int.*, 1993, vol. 33, pp. 619-39.
42. C. Beckermann and C.Y. Wang: in *Annual Review of Heat Transfer*, C.L. Tien, ed., Begell House, New York, NY, 1995, vol. VI, pp. 115-98.

43. J. Ni and C. Beckermann: *Metall. Trans. B*, 1991, vol. 22B, pp. 349-61.
44. C.Y. Wang and C. Beckermann: *Metall. Mater. Trans. A*, 1996, vol. 27A, pp. 2754-64.
45. C.Y. Wang and C. Beckermann: *Metall. Trans. A*, 1993, vol. 24A, pp. 2787-2802.
46. J.D. Hunt: *Solidification and Casting of Metals*, Metals Society, London, 1979.
47. J.F. Richardson and W.N. Zaki: *Trans. Inst. Chem. Eng.*, 1954, vol. 32, pp. 35-53.
48. J. Happel: *AIChE J.*, 1958, vol. 4, pp. 197-201.
49. E. Barnea and J. Mizrahi: *Chem. Eng. J.*, 1973, vol. 5, pp. 171-89.
50. J. Garside and M.R. Al-Dibouni: *Ind. Eng. Chem. Process Des. Dev.*, 1977, vol. 16, pp. 206-14.
51. A.R. Khan and J.F. Richardson: *Chem. Eng. Comm.*, 1989, vol. 78, pp. 111-30.
52. R.B. Bird, W.E. Stewart, and E.N. Lightfoot: *Transport Phenomena*, John Wiley & Sons, New York, NY, 1960.
53. C.Y. Wang, S. Ahuja, C. Beckermann, and H.C. de Groh: *Metall. Mater. Trans. B*, 1994, vol. 26B, pp. 111-19.
54. M. Hassanizadeh and W. Gray: *Adv. Water Resources*, 1980, vol. 3, pp. 25-40.
55. M.C. Bhat: Ph.D. Thesis, The University of Arizona, Tucson, AZ, 1995.
56. Y.T. Shih, D. Gidaspow, and D.T. Wasan: *Powder Technol.*, 1987, vol. 50, pp. 201-15.
57. D.J. Jeffrey and A. Acrivos: *AIChE J.*, 1976, vol. 22, pp. 417-32.
58. J.F. Brady and G. Bossis: *J. Fluid Mech.*, 1985, vol. 155, pp. 105-29.
59. A.B. Metzner: *J. Rheology*, 1985, vol. 29, pp. 739-75.
60. H.N. Stein: *Encyclopedia of Fluid Mechanics*, Slurry Flow Technology, Gulf Publishing Company, Houston, TX, 1986, vol. 5, ch. 1.
61. R.H. Davis: *Adv. Coll. Interface Sci.*, 1993, vol. 43, pp. 17-50.
62. R. Mehrabian, R.G. Riek, and M.C. Flemings: *Metall. Trans.*, 1973, vol. 5, pp. 1899-1905.
63. F.A. Girot, L. Albingre, J.M. Quenisset, and R. Naslain: *JOM*, 1987, Nov., pp. 18-21.
64. H.K. Moon, J.A. Cornie, and M.C. Flemings: *Mater. Sci. Eng. A*, 1991, vol. A144, pp. 253-65.
65. A. Einstein: *Ann. Phys.*, 1905, vol. 17, p. 549.
66. D.G. Thomas: *J. Coll. Sci.*, 1965, vol. 20, pp. 267-77.
67. B.K. Dhindaw, A. Moitra, D.M. Stefanescu, and P. Curreri: *Proc. 2nd Int. Symp. on Experimental Methods for Microgravity Materials Science Research*, R.A. Schiffman, ed., TMS, Warrendale, PA, 1988, pp. 123-28.
68. I.M. Krieger: *Adv. Coll. Interface Sci.*, 1972, vol. 3, pp. 111-36.
69. D.M. Stefanescu, F. Rana, A. Moitra, and S. Kacar: in *Solidification of Metal Matrix Composites*, P. Rohatgi, ed., TMS, Warrendale, PA, 1990, pp. 77-89.
70. A. Moitra, B.K. Dhindaw, and D.M. Stefanescu: in *Solidification of Metal Matrix Composites*, P. Rohatgi, ed., TMS, Warrendale, PA, 1990, pp. 91-101.
71. P.K. Rohatgi, R. Asthana, and F. Yarandi: in *Solidification of Metal Matrix Composites*, P. Rohatgi, ed., TMS, Warrendale, PA, 1990, pp. 51-76.
72. C.S. Wang, R.W. Lyczkowski, and G.F. Berry: *3rd Int. Symp. on Liquid-Solid Flows*, M.C. Roco, ed., ASME, Chicago, IL, 1988, pp. 29-35.
73. J. Ni and C. Beckermann: *J. Mater. Processing Manufacturing Sci.*, 1993, vol. 2, pp. 217-31.
74. R.J. Feller: Ph.D. Thesis, The University of Iowa, Iowa City, IA, 1996.
75. D.B. Spalding: *Numerical Properties and Methodologies in Heat Transfer*, Proc. *2nd Nat. Symp.*, T.M. Shih, ed., Hemisphere Publishing, Washington, DC, pp. 421-36.
76. C. Prakash and V. Voller: *Num. Heat Transfer*, 1989, vol. 15, pp. 171-89.
77. M.C. Schneider and C. Beckermann: Technical Report No. UIME-CB01-1993, The University of Iowa, Iowa City, IA, 1993.
78. C.Y. Wang and C. Beckermann: *Metall. Mater. Trans. A*, 1996, vol. 27A, pp. 2765-83.
79. M.C. Schneider and C. Beckermann: *Int. J. Heat Mass Transfer*, 1995, vol. 38, pp. 3455-73.
80. J. Ding and D. Gidaspow: *AiChE J.*, 1990, vol. 36, pp. 523-38.
81. W. Kurz and D.J. Fisher: *Fundamentals of Solidification*, Trans Tech Publications, Aedermannsdorf, Switzerland, 1989.
82. S. Gowri and F.H. Samuel: *Metall. Trans. A*, 1992, vol. 23A, pp. 3369-76.
83. R. Glauner, M.A.W. Barnick, and H. Lehl: *Gmelins Handbuch der Anorganischen Chemie*, Auflage 8, System-Nummer 35: Aluminium, Teil A. Lieferung 4, Verlag Chemie, GmbH, Berlin, 1936.
84. R.J. Feller and C. Beckermann: *Int. Comm. Heat Mass Transfer*, 1993, vol. 20, pp. 311-22.
85. C.J. Smithells: *Metals Reference Book*, Butterworth and Co., London, 1976.
86. H. Landolt and R. Börnstein: *Zahlenwerte und Funkt.*, Springer-Verlag, Berlin, 1965, Teil 2, Band IV.
87. Ph. Thévoz, J.L. Desbiolles, and M. Rappaz: *Metall. Trans. A*, 1989, vol. 20A, pp. 311-22.
88. M. Rappaz and Ph. Thévoz: *Acta Metall.*, 1987, vol. 35, pp. 1487-97.
89. H. Landolt and R. Börnstein: *Zahlenwerte und Funktionen*, Springer-Verlag, Berlin, 1968, Teil 5, Band II.
90. L.F. Mondolfo: *Aluminum Alloys: Structure and Properties*, Butterworth and Co., London, 1976.